Stem Cell Reports
Report
ISSCR
OPEN ACCESS

The tumor suppressor WT1 drives progenitor cell progression and epithelialization to prevent Wilms tumorigenesis in human kidney organoids

Verena Waehle,[1,2] Rosemarie Ungricht,[3] Philipp S. Hoppe,[3] and Joerg Betschinger[1,4,*]
[1]Friedrich Miescher Institute for Biomedical Research, 4058 Basel, Switzerland
[2]Faculty of Sciences, University of Basel, 4003 Basel, Switzerland
[3]Novartis Institutes for BioMedical Research, Novartis Pharma AG, 4056 Basel, Switzerland
[4]Lead contact
*Correspondence: joerg.betschinger@fmi.ch
https://doi.org/10.1016/j.stemcr.2021.07.023

SUMMARY

Wilms tumor is the most widespread kidney cancer in children and frequently associated with homozygous loss of the tumor suppressor *WT1*. Pediatric tumorigenesis is largely inaccessible in humans. Here, we develop a human kidney organoid model for Wilms tumor formation and show that deletion of *WT1* during organoid development induces overgrowth of kidney progenitor cells at the expense of differentiating glomeruli and tubules. Functional and gene expression analyses demonstrate that absence of *WT1* halts progenitor cell progression at a pre-epithelialized cell state and recapitulates the transcriptional changes detected in a subgroup of Wilms tumor patients with ectopic myogenesis. By "transplanting" *WT1* mutant cells into wild-type kidney organoids, we find that their propagation requires an untransformed microenvironment. This work defines the role of WT1 in kidney progenitor cell progression and tumor suppression, and establishes human kidney organoids as a phenotypic model for pediatric tumorigenesis.

INTRODUCTION

Tumor initiation and progression are typically studied in genetically engineered mice (Kersten et al., 2017), whose relevance to human disease is limited by species- and strain-specific mechanisms, and the artificial induction of multiple oncogenes at the same time. Most human cancer models, including cell lines grown on tissue plastic or as patient-derived xenografts in mice (Hynds et al., 2018) employ patients' cells that are derived from tumor resections or biopsies, typically at a late stage of the disease. Such systems depend on prolonged culture under non-physiological conditions that alter tumor cell properties and result in poor clinical predictiveness. Patient tumor-derived organoids, in contrast, preserve tumor heterogeneity, stages of tumor progression, and drug responses. Furthermore, engineering of cancer lesions into wild-type organoids induces cancer-specific transcriptional changes and predisposes to tumor formation upon xenotransplantation (Clevers and Tuveson, 2019). Organoids may therefore be suitable to study mechanisms of tumor initiation and progression.

Wilms tumor (WT) is the most common kidney cancer in childhood and accounts for 7% of all pediatric cancers (Treger et al., 2019). Stalled nephrogenesis is thought to be the major cause of disease. This is supported by the transcriptional similarity of WT to fetal cell types and by the function of several WT oncogenes and tumor suppressors in normal kidney development (Treger et al., 2019). WT patients show mutations in a diverse set of genes, including homozygous inactivation of the tumor suppressor Wilms tumor 1 (*WT1*) (Schumacher et al., 1997) and neomorphic mutations in genes encoding the kidney transcription factors (TFs) SIX1 and SIX2. Gene expression analysis has suggested that Wilms tumorigenesis initiates in distinct cell types of origin and is influenced not only by which genes or pathways are mutated but also by the developmental context in which genetic lesions occur (Gadd et al., 2012).

Here, we exploited human kidney organoids to study mechanisms of WT initiation and progression. We showed that genetic knockout (KO) of *WT1* induces overgrowth of nephron progenitor cells (NPCs) at the expense of tubular and glomerular differentiation. Further characterization revealed progression into an organoid state that transcriptionally and phenotypically resembles a subset of WT patients, as well as arrest of NPC differentiation at a pre-epithelialized cell state. Our study therefore defines WT1-mediated developmental cell fate transitions that drive organogenesis and protect from hyperplasia, and establishes modeling of Wilms tumorigenesis in human kidney organoids.

RESULTS

WT1 deletion inhibits NPC epithelialization and differentiation and induces organoid hyperplasia

We generated kidney organoids using an adaptation (Ungricht et al., 2021) of a two-step differentiation protocol (Morizane et al., 2015) (Figure S1A). Organoids contained podocytes that express WT1, PODXL, and NPHS1, and epithelial tubule cells that express high levels of EPCAM

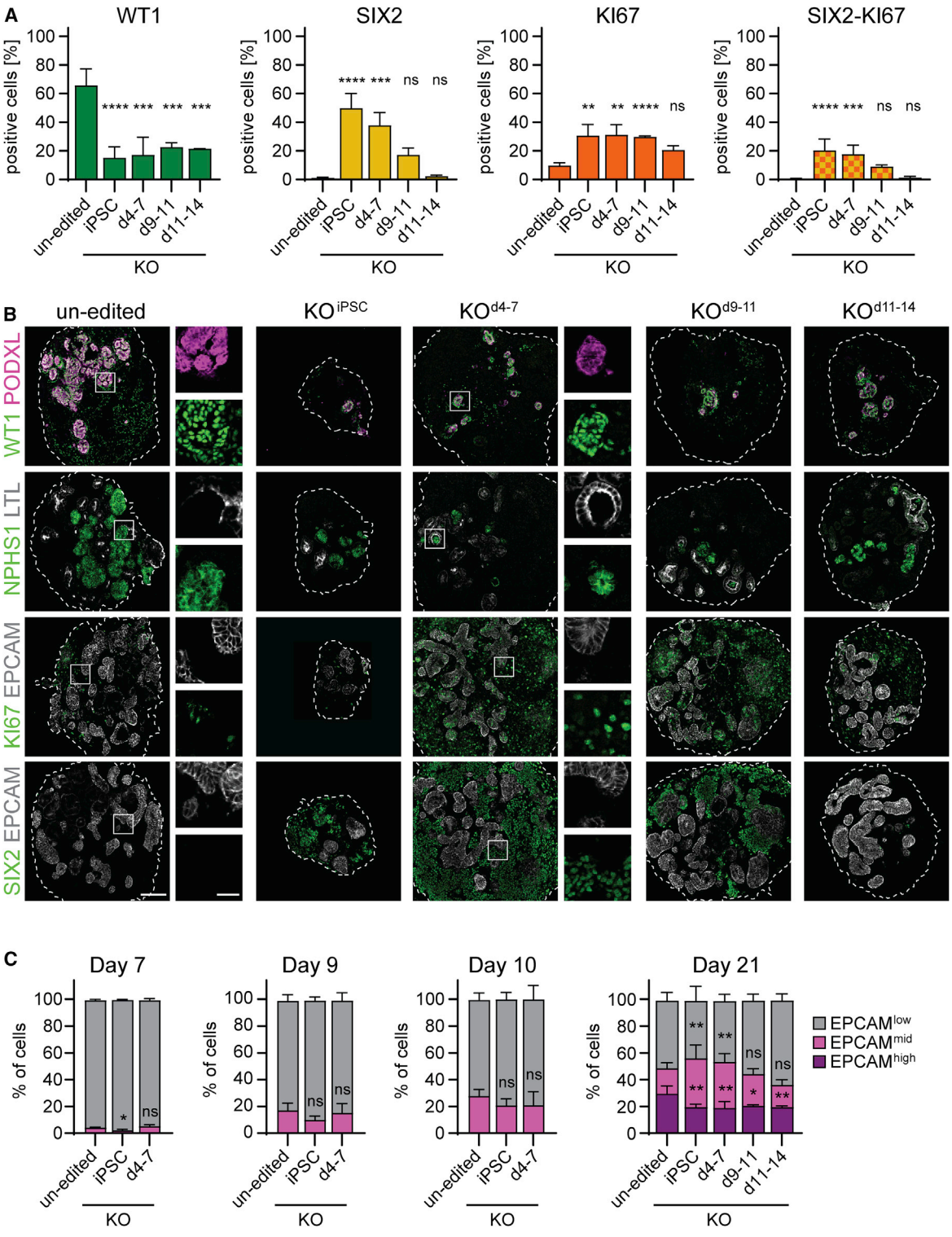

Figure 1. Loss of *WT1* induces NPC overgrowth

(A) Quantification of subpopulations in un-edited, KO^{iPSC}, KO^{d4-7}, KO^{d9-11}, and KO^{d11-14} d21 organoids by flow cytometry of indicated markers. Data are presented as mean percentage of positive cells ± SD derived from n = 5 (un-edited, KO^{iPSC}, KO^{d4-7}) or n = 2 (KO^{d9-11}, KO^{d11-14}) independent experiments. Two-sided Student's t test; p value: ns, > 0.05; * ≤0.05; ** ≤0.01; *** ≤0.001; **** ≤0.0001.

(legend continued on next page)

(EPCAM^{high}) with distal and proximal segments additionally labeled by CDH1 and LTL, respectively (Figures S1B and S1C). For KO of *WT1* we infected induced pluripotent stem cells (iPSCs) harboring a doxycycline (DOX)-inducible Cas9 protein (WT29-iCas9) (Figures S1D and S1E) (Ungricht et al., 2021) with lentiviruses driving expression of a *WT1*-specific guide RNA (gRNA1) and a red fluorescent protein (RFP). We induced genome editing by adding DOX at different stages of kidney organoid differentiation: in iPSCs prior to differentiation (KO^{iPSC}), during intermediate mesoderm specification (KO^{d4-7}), during NPC differentiation (KO^{d9-11}), and during nephrogenesis (KO^{d11-14}). To determine KO efficiency and kinetics, we quantified WT1 protein by flow cytometry. This showed that KO^{iPSC} and KO^{d4-7} impaired the steep increase of WT1-expressing cells between day (d) 5 and d6 of organoid formation, resulting in an approximate 80% and 70% reduction of the WT1-positive cell fraction by d9, respectively (Figures S1F and S1G). Although not as efficient, loss of WT1 upon KO^{d9-11} and KO^{d11-14}, similar to KO^{d4-7}, occurred between 24 h and 48 h after Cas9 induction.

At d21, control and *WT1* mutant organoids were of similar size, except for those derived from KO^{iPSC} cells, which were considerably smaller (Figure S2A). Culture until d30 showed that KO^{iPSC} organoids remained small, that KO^{d4-7} and KO^{d9-11} organoids overgrew, and that growth of KO^{d11-14} organoids was similar to controls. Profiling with cell-type-specific markers at d21 (Figures 1A, 1B, and S2B) revealed that SIX2-positive (SIX2^{pos}) cells were abundant in KO^{iPSC} and KO^{d4-7} organoids (50% and 38% of all cells, respectively), and absent from KO^{d11-14} organoids similar to controls. In addition, the proliferation marker KI67 was elevated, in particular upon KO^{iPSC} and KO^{d4-7}. Many KI67-positive (KI67^{pos}) cells co-expressed SIX2, suggesting overgrowth of NPCs. KO^{d9-11} organoids displayed intermediate phenotypes that frequently did not differ significantly from controls.

PODXL- and NPHS1-expressing podocytes were strongly reduced in all *WT1* mutant organoids, including KO^{d11-14} organoids (Figure 1B). Strikingly, the few detectable PODXL-positive cells co-expressed WT1, demonstrating that they are descendants of un-edited or heterozygous mutant NPCs or of NPCs harboring in-frame *WT1* mutations. EPCAM^{high} and LTL-positive (LTL^{pos}) tubules were reduced, indicating impaired formation of tubules (Figures 1B and 1C). We estimate that approximately 15% of WT1-deficient cells expressed EPCAM^{high} (Figure S2C). This was lower than un-edited control organoid cells (30%), confirming reduced epithelialization. Defective nephrogenesis was also observed in KO^{d11-14} organoids, in which exit from the SIX2^{pos} state was unperturbed, indicating that *WT1* drives NPC, and proximal tubule and podocyte differentiation through successive mechanisms. We sought to validate these findings with two independent *WT1* gRNAs and found a reduction of WT1 and EPCAM^{high}, maintenance of SIX2, elevation of KI67, and co-expression of SIX2 and KI67 in KO^{iPSC} organoids. Notably, phenotypic strength scaled with the KO efficiency of the respective gRNA, demonstrating target specificity (Figures S2D and S2E).

While quantifying EPCAM expression, we found an expansion of EPCAM^{mid} cells in KO^{iPSC} and KO^{d4-7} d21 organoids (Figures 1C, S2C, S2F, and S2G). A proportion of these cells expressed SIX2 (33% and 26%, respectively). KO^{d11-14} organoids, in contrast, were indistinguishable from controls. Immunofluorescence confirmed expression of EPCAM in SIX2^{pos} cells at lower levels than in fully differentiated tubules and not confined to the basolateral membrane (Figure S2H). Consistent with an epithelializing intermediate state, these structures also expressed low levels of CDH1 (Figure S2H). EPCAM^{mid} cells emerged as early as d7 and preceded the formation of EPCAM^{high} cells (Figure 1C). These cells are therefore likely equivalent to EPCAM^{dim} cells in the human fetal kidney (Pode-Shakked et al., 2017), which are kidney progenitor intermediates undergoing a mesenchymal-epithelial transition (MET) and bridging the differentiation of EPCAM^{low} NPCs into EPCAM^{high} renal vesicle cells. The frequency of EPCAM^{mid} cells, in particular of those co-expressing SIX2, increased steadily in developing KO^{iPSC} and KO^{d4-7} organoids (Figure S2I), suggesting that WT1 promotes progression beyond a pre-epithelial SIX2^{pos}/EPCAM^{mid} NPC transition state, but not the initiation of MET.

We noted increased SIX2 protein levels in NPCs at d9 (Figure S2J). To test if this is causal for progenitor overgrowth, we generated iPSCs with a DOX-inducible mCherry::T2A::SIX2 transgene and induced SIX2 by adding DOX from d7 and d9 onwards, thus initiating overexpression in NPCs and during nephrogenesis, respectively (Figures S2K and S2L). The former resulted in smaller organoids that, compared with uninduced controls, had fewer EPCAM^{high} and LTL^{pos} tubules and WT1-positive glomeruli

(B) Staining of indicated markers in representative d21 organoids as in (A). Scale bar: 100 μm. White boxed regions are shown as blow-ups. Scale bar: 25 μm.

(C) Flow cytometry-based quantification of EPCAM^{high}, EPCAM^{mid}, and EPCAM^{low} populations (gating shown in Figure S2G) in organoids of indicated time points and genotypes. Data are shown as mean percentage of positive cells ± SD derived from n = 3 (d7); n = 4 (d9); n = 2 (d10); n = 5 (un-edited, KO^{iPSC}, KO^{d4-7}; d21) or n = 2 (KO^{d9-11}, KO^{d11-14}; d21) independent experiments. Two-sided student's t test; p value: ns > 0.05; * ≤ 0.05; ** ≤ 0.01; asterisks are placed above the respective populations (EPCAM^{high} and EPCAM^{mid}).

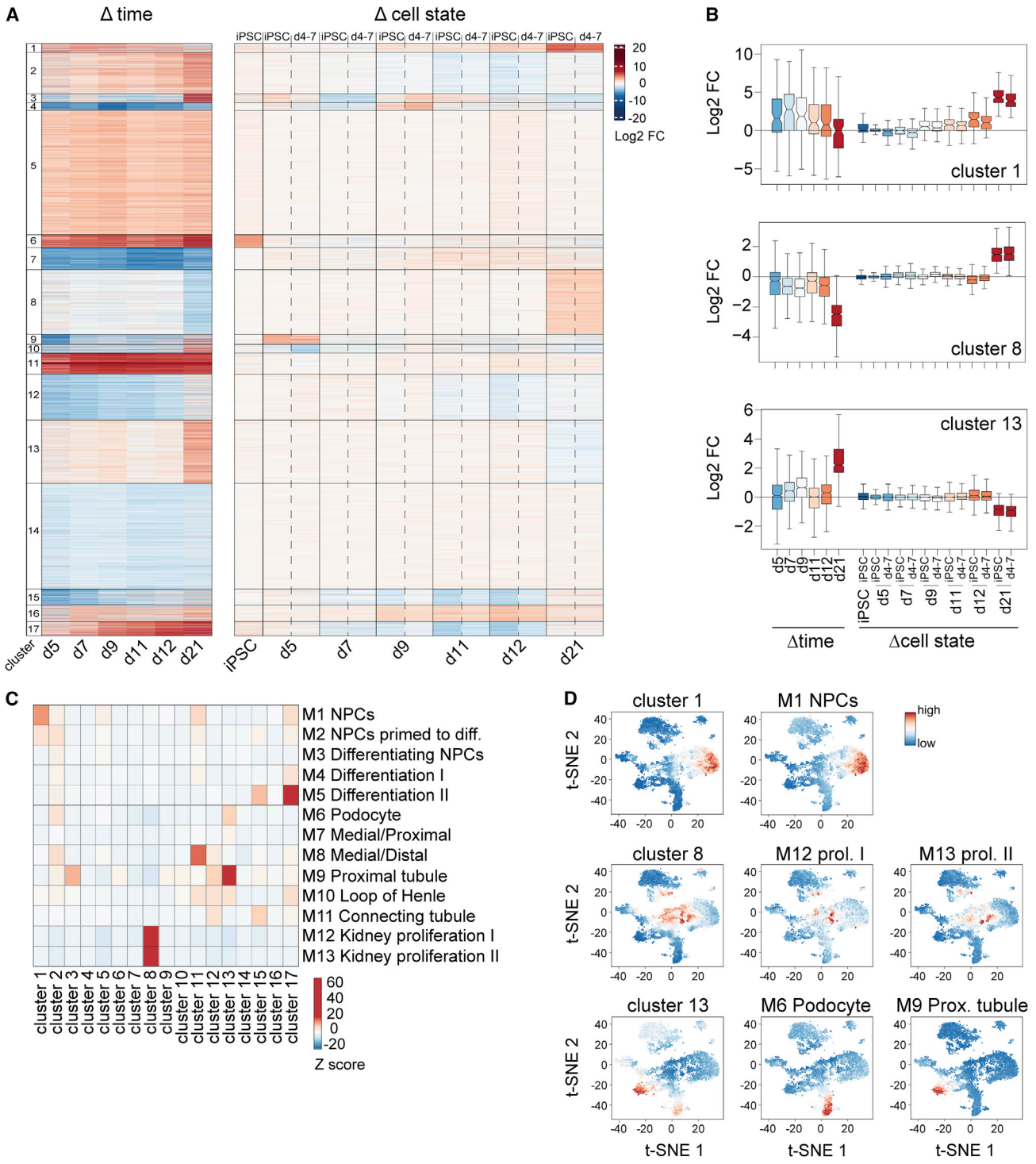

Figure 2. Absence of *WT1* impairs developmental transcription

(A) k-means clustering of 7,626 genes significantly changing in any of the shown contrasts. Left: time course of wild-type organoid development; log2-fold expression changes relative to iPSCs. Right: changes in KO^{iPSC} or KO^{d4-7} cells at indicated time points; log2-fold expression changes relative to un-edited control at each time point. log2 FC = log2-fold change.

(B) Quantification of mRNA log2-fold expression changes of indicated gene clusters and in contrasts as specified in (A).

(legend continued on next page)

(Figures S2M and S2N). Quantitative PCR (qPCR) showed that SIX2 was expressed roughly 30-fold higher in d7-induced NPCs than in uninduced controls (Figure S2K). In both, d7- and d9-induced organoids, however, KI67 expression was unchanged. SIX2, despite heterogeneous and mosaic expression, was detectable in differentiated EPCAM^{high} and LTL^{pos} tubule cells at d21 (Figure S2N).

Taken together, these observations suggest that the removal of *WT1* impairs NPC progression and leads to organoid hyperplasia. We found that over-activation of SIX2 was not sufficient to recapitulate these phenotypes (Figures S2K–S2N), arguing for additional WT1 targets. Tubule and podocyte differentiation defects in KO$^{d11\text{-}14}$ organoids indicate roles of WT1 in nephrogenesis that are independent of SIX2 silencing and consistent with WT1 activating podocyte-specific genes (Kann et al., 2015) and promoting epithelial tubule maturation (Berry et al., 2015).

WT1 drives developmental transcription

We decided to define the transcriptional changes induced by absence of *WT1*, and performed RNA sequencing (RNA-seq) of KO^{iPSC} and KO$^{d4\text{-}7}$ cells and respective controls at different time points during organoid development (Figure S3A). Inspection of cell state-specific markers (Figures S3B–S3D) revealed consistency between transcriptional and phenotypic changes: (1) NPC markers were induced by d5 and declined after d9 in control organoids but persisted upon KO of *WT1*; (2) markers of differentiation intermediates, and of mature podocytes and proximal tubules, were induced by d9 and d21 in un-edited controls, respectively, which was impaired in mutant organoids; and (3) transcriptional dynamics of epithelial-mesenchymal transition (EMT) signature genes, including EPCAM and CDH1, were perturbed in KO organoids.

To systematically define WT1-dependent gene regulation, we performed k-means clustering of transcripts that change significantly during organoid development and/or in KO organoids (Figures 2A and 2B Table S1). This identified 17 gene clusters, of which some were induced or repressed during organoid development and unchanged in mutants (clusters 5, 7, 11, and 14), while others were deregulated in KO organoids, in particular at d21 (clusters 1, 8, and 13). Notably, we did not identify clusters that were mis-regulated across all time points, suggesting that WT1's target genes depend on the developmental context. Also, expression defects in KO^{iPSC} and KO$^{d4\text{-}7}$ organoids, despite distinct growth rates (Figure S2A), were very similar, and indistinguishable at d21.

Because of the differentiation defects in *WT1* KO organoids, we wondered if any of the gene clusters reflect cell-type-specific transcription. We made use of published gene sets that discriminate cell types of the human fetal kidney (Lindström et al., 2018) and calculated gene set overlap enrichments (see supplemental experimental procedures). This identified gene clusters 1, 8, 11, 13, and 17 to be most similar to markers of relevant cell types in the developing kidney (Figure 2C). Notably, cluster 11 was not changed, and cluster 17 only transiently deregulated in KO organoids (Figure 2A, Table S1). We validated cell type specificity of clusters 1, 8, and 13 genes by visualizing their expression in t-distributed stochastic neighbor embedding (t-SNE) maps of single-cell RNA-seq (scRNA-seq) of the week 16 human fetal kidney (Hochane et al., 2019). This confirmed co-expression with gene sets of kidney progenitor cells (M1), proliferating intermediates (M12 and M13), and podocytes (M6) and proximal tubule cells (M9), respectively (Figure 2D).

Collectively, the transcriptional defects correlate with the phenotypic persistence of kidney progenitor cells (cluster 1) and reduced tubular and glomerular formation (cluster 13) in mutant organoids. The specificity of the former to *WT1* depletion before d11 (Figures 1A, 1B, S2A, S2B, S2C, S2F) is consistent with WT1 acting in and driving differentiation of NPCs. Although we cannot exclude that upregulation of cluster 8 genes in mutant organoids reflects growth of a proliferating transit amplifying cell population, we note (1) that cluster 8 genes are downregulated specifically at d21, suggesting cell type-independent transcription (Figures 2B and S3E); and (2) that a significant proportion of SIX2^{pos} cells co-express KI67 (Figure 1A), whose encoding gene *MKI67* is a cluster 8 gene (Table S1). Upregulation of cluster 8 genes is therefore likely due to NPC hyperproliferation rather than the persistence of an additional transit amplifying cell population.

WT1 KO organoids recapitulate transcriptional changes in Wilms tumors

To explore the similarity of *WT1* KO kidney organoids and kidney tumors, we compared transcriptional changes in mutant d21 organoids with mean gene expression changes in WT (Gadd et al., 2017), kidney chromophobe tumor (KICH) (Davis et al., 2014), kidney renal papillary cell carcinoma (KIRP) (Network et al., 2016), and kidney renal clear cell carcinoma (KIRC) (Creighton et al., 2013) patients. This showed that the magnitude and the directionality of cluster 1 and 8 deregulation was conserved in WT but not

(C) Gene set overlap significance scores (see supplemental experimental procedures) of 17 gene clusters with fetal kidney cell type gene sets as defined in Lindström et al. (2018). Z scores are color coded. Diff, differentiate.
(D) t-SNE maps of scRNA-seq data from week 16 human fetal kidney (Hochane et al., 2019). Expression levels of indicated clusters and gene sets as in (C) are color-coded. prol, proliferation; Prox, proximal.

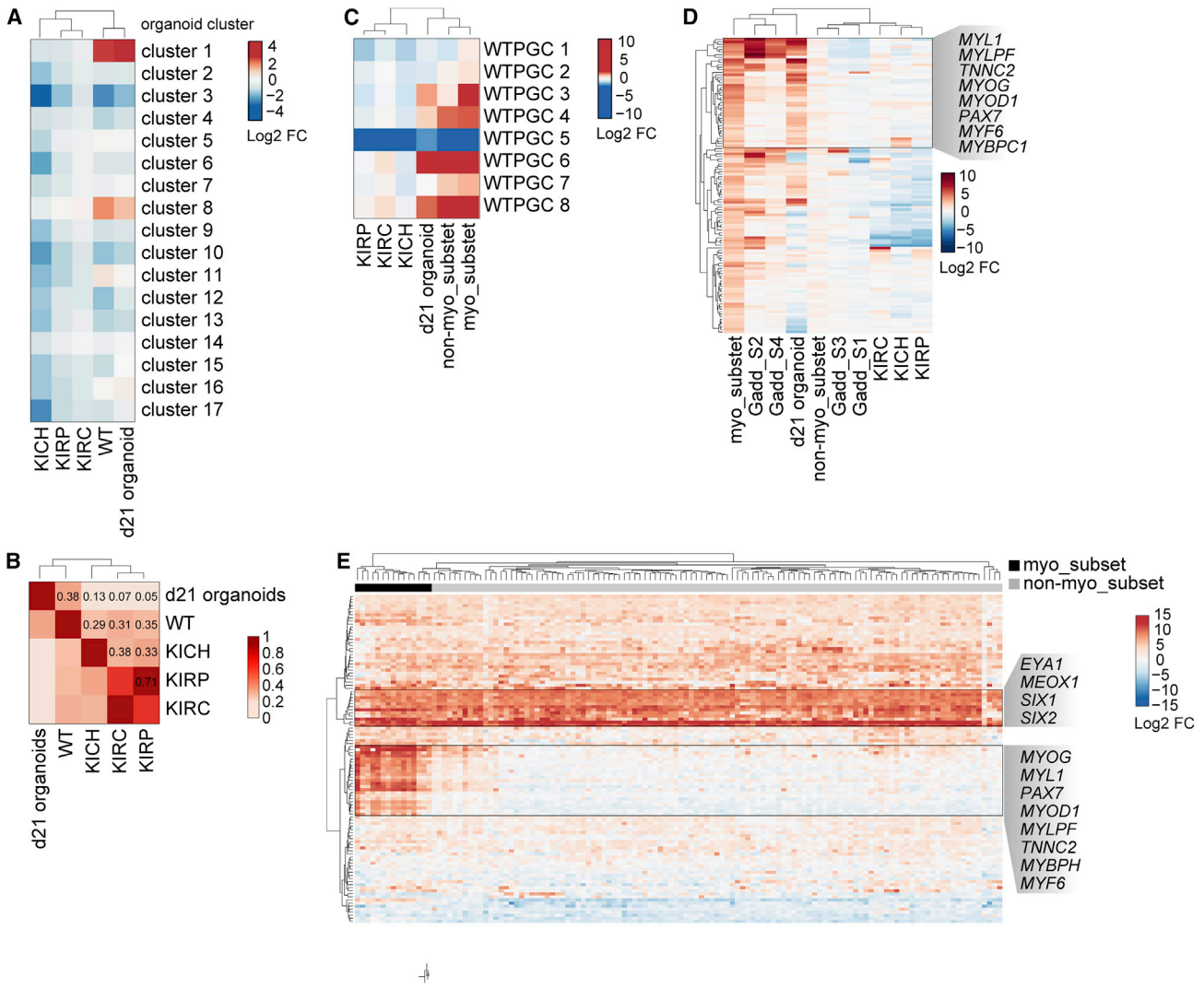

Figure 3. *WT1* KO organoids recapitulate the transcriptional changes of a Wilms tumor patient subgroup

(A) Unsupervised clustering of mean expression changes of clusters 1–17 in organoids and kidney tumors. Mean log2-fold expression changes in KO^{iPSC} and KO^{d4-7} organoids relative to un-edited controls and in patient tumors relative to control tissue were used.

(B) Pearson correlation coefficients and unsupervised clustering of pairwise comparisons between scaled mean log2-fold expression changes as described in (A).

(C) Unsupervised clustering of mean expression changes of WTPGCs 1–8 in organoids and kidney tumors. Scaled mean log2-fold expression changes as described in (A) were used. myo_subset and non-myo_subset are the subsets of WT patients defined in Figure S3G.

(D) Unsupervised clustering of scaled mean log2-fold expression changes of WTPGC 3 genes as in (C). Gadd_1/2/3/4 are mean-centered scaled expression changes of WT patient subsets defined in Gadd et al. (2012). Cluster containing muscle genes is highlighted.

(E) Unsupervised clustering of log2-fold expression changes of cluster 1 genes in individual WT patients relative to corresponding normal tissue. Clusters containing NPC and muscle genes are highlighted.

KICH, KIRP, or KIRC tumors (Figure 3A). Pairwise comparison of transcriptome-wide changes confirmed that changes in mutant d21 organoids correlate most strongly with those of WT patients (Figure 3B). *WT1* KO kidney organoids therefore resemble WT patient tissue, despite being derived *in vitro* and consisting of nephron cell types only (Morizane et al., 2015).

Using gene ontology (GO) analysis (Table S1) we found enrichment of cell cycle terms in cluster 8, while cluster 1, despite containing key NPC TFs such as SIX1 and SIX2, was highly enriched for muscle-related processes (Figure S3F). Notably, *WT1* mutations are associated with ectopic myogenesis in mice and in WT patients (Berry et al., 2015; Gadd et al, 2012, 2017; Miyagawa et al.,

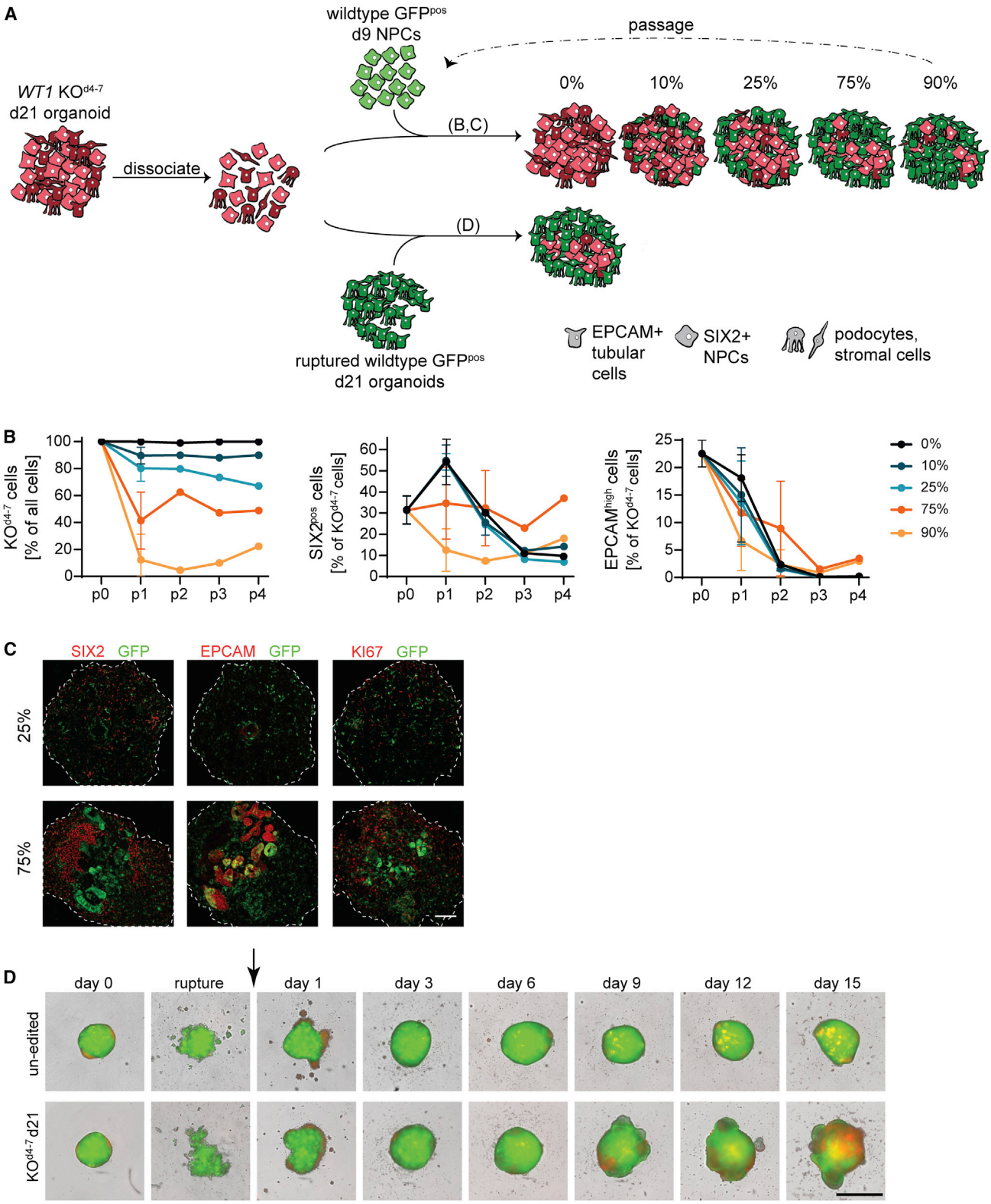

(legend on next page)

1998). To test if *WT1* KO organoids resemble this patient subset, we first stratified WT patients by gene expression. Using k-means clustering (Figure S3G, Table S2), we identified several WT patient gene clusters (WTPGCs), including WTPGCs 6 and 8, that were deregulated in all 126 WT patients (Gadd et al., 2017) and enriched for developmental and cell cycle terms, respectively (Figure S3H, Table S2). WTPGC 3, in contrast, was upregulated in a subgroup of 15 patients only (myo_subset), enriched for muscle GO terms (Figure S3H), induced in previously described myogenic S2 and S4 WT patient subgroups (Gadd et al., 2012) (Figure S3I), and upregulated in d21 KO organoids (Figures 3C and 3D). Vice versa, unsupervised clustering of cluster 1 genes in WT patients (Figure 3E) identified NPC TFs upregulated in all samples, while the myogenic TFs *MYOD1* and *MYOG*, and the skeletal muscle genes *TNNC2* and *MYLPF*, were specifically dysregulated in the myo_subset of patients. We therefore conclude that transcriptional changes in *WT1* mutant kidney organoids recapitulate those of a myogenic subset of WT patients.

Niche signals propagate *WT1* mutant NPCs

The persistence of SIX2^{pos} cells and NPC transcription in *WT1* KO organoids may result from a block or a delay in developmental progression. We reasoned that serial passaging in differentiation-promoting conditions would discriminate between the two by enforcing the commitment of delayed but not of blocked mutant cells. To do so, we aggregated single cells derived from KO$^{d4\text{-}7}$ d21 organoids and exposed them to organoid-forming conditions for 12d (corresponding to d9–d21 of iPSC differentiation), and repeated this procedure for up to four passages (Figure 4A). Since niche signals affect tumor growth and progression (Hanahan and Coussens, 2012), we also tested the role of environment signaling in passaging of SIX2^{pos} cells. We therefore added defined ratios (0%, 10%, 25%, 75%, and 90%) of green fluorescent protein (GFP)-expressing wild-type d9 NPCs to dissociated KO$^{d4\text{-}7}$ organoids during the aggregation step at the beginning of each passage, expecting that the wild-type kidney structures formed by these NPCs would provide niche signals to KO cells. Quantifying the percentage of GFP-expressing cells in chimeric organoids (Figure 4B) showed stable contribution of KO cells over passages, demonstrating that KO$^{d4\text{-}7}$ d21 organoid cells grew as fast as wild-type d9 NPCs. Un-edited control d21 organoid cells proliferated less (Figure S4A). The mutant cell type composition, in contrast, varied across passages and mixing ratios (Figures 4B, 4C, and S4B): in the absence (0%) or presence of 10% and 25% wild-type cells, the fraction of SIX2^{pos} cells increased from approximately 30% to 60% after the first passage, but gradually declined during further passaging. Un-edited control cells, in contrast, did not gain SIX2 expression (Figure S4C). In the presence of 75% wild-type cells, the percentage of SIX2^{pos} cells remained at 30% over passages for at least 60d. Presence of 90% wild-type cells stabilized SIX2-expression in 10% of KO$^{d4\text{-}7}$ cells after the first passage. Therefore, signals by wild-type cells, particularly at a wild-type/mutant cell ratio of 3:1, support self-renewal of KO$^{d4\text{-}7}$ SIX2^{pos} cells. At and below mixing ratios of 1:3, SIX2^{pos} cells were lost during passaging. This was not accompanied by an induction of EPCAM^{high} cells (Figure 4B) and therefore not due to overt tubular differentiation.

Passaging in the presence of wild-type NPCs is not comparable with growth in mature tissues, such as during tumor progression in patients or in patient-derived xenograft mouse models. We therefore decided to use ruptured GFP-expressing d21 organoids as a differentiated cell substrate for passaging of *WT1* mutant cells (Figure 4A). We estimated that d21 organoids contain 150,000–200,000 cells, to which we added 12,500 and 25,000 cells of RFP-expressing control or mutant single cells, corresponding to a mixing ratio of approximately 80%–90%. KO$^{d4\text{-}7}$ d21 cells expanded visibly (Figure 4D), expressed SIX2 and KI67, and caused chimeric organoid overgrowth (Figures 4D, S4D, and S4E). In contrast, un-edited d21 cells contributed poorly to organoids. To exclude that this is because of poor survival upon dissociation or reaggregation, we used un-edited d9 NPCs as control, and found that they integrated as well as KO$^{d4\text{-}7}$ d21 cells and contributed efficiently to EPCAM-positive epithelia. However, these cells did not induce organoid overgrowth or maintain SIX2 expression (Figures S4D–S4F). Passaging in d21 kidney organoids therefore enables persistence of SIX2 and proliferation of

Figure 4. Non-cell-autonomous regulation of self-renewal and heterogeneity

(A) Schematic of the experimental flow.

(B) Quantification of indicated cell populations in chimeric organoids after passaging with indicated ratios of wild-type GFP-expressing d9 NPCs and at indicated passages. p0 indicates KO$^{d4\text{-}7}$ d21 organoids that were used as starting material for passaging. Data are shown as mean percentage ± SD from n = 1 or 2 independent experiments. Percentage of all cells is relative to all cells of chimeric organoids, and percentage of KO$^{d4\text{-}7}$ cells is relative to all mutant cells, therefore excluding wild-type host cells.

(C) Staining at p3 of indicated markers and mixing ratios as outlined in (A). Scale bar: 100 μm.

(D) Images of organoids obtained after adding 12,500 RFP-positive un-edited d21 organoid cells (top) and KO$^{d4\text{-}7}$ d21 organoid cells (bottom) to ruptured wild-type GFP-expressing organoids. Images were recorded at indicated time points using an Incucyte system. Scale bar: 1 mm.

WT1 mutant cells. Notably this did not require extrinsic CHIR and FGF9 (Figures S4G–S4I), and is therefore independent of differentiation- and growth-promoting culture conditions.

We conclude that kidney organoids can be exploited for tumor cell transplantation and growth in a developmental (d9 NPCs) and mature (d21 organoids) tissue context. Our observations suggest cell-autonomous and non-cell-autonomous mechanisms that drive the ectopic growth of mutant NPCs, specifically a developmental block induced by absence of *WT1* and pro-self-renewal signals from a wild-type niche environment.

DISCUSSION

WT1 mutations in humans predispose to familial forms of WT and are found in 10%–20% of sporadic WT patients (Hastie, 2017; Treger et al., 2019). Loss of *WT1* in humans is thought to transform immature kidney progenitor cells (Treger et al., 2019). However, direct evidence for a role of WT1 in human NPC development is elusive. Using timed deletion in human iPSC-derived kidney organoids, we identified two successive functions of WT1: driving exit from the NPC state and MET, and podocyte and tubule differentiation.

The second, later, function is reminiscent of the role of mouse *Wt1* in glomerulus and renal tubule development (Berry et al., 2015; Kann et al., 2015), suggesting that WT1 promotes lineage progression through conserved target genes, such as podocyte-specifying TFs (Kann et al., 2015). The first, earlier, function of *WT1* appears less conserved in organoids, although it remains to be determined if this is due to actual species-specific mechanisms or different experimental settings: (1) early deletion of *Wt1* in mice results in an expansion of mesenchymal cells, but not in ectopic NPC marker expression or tumor formation (Berry et al., 2015; Huang et al., 2016), while KO of *WT1* in organoids was sufficient for SIX2^{pos} cell overgrowth. (2) Early deletion of *Wt1* in mice blocks MET and, consequentially, formation of CDH1-expressing tubule cells (Berry et al., 2015). Accumulation of SIX2^{pos} cells co-expressing EPCAM^{mid} in KO organoids indicates that human WT1 coordinates NPC differentiation and epithelialization, too. However, the perturbed transcriptional induction of MET genes *WNT4*, *CDH1*, *EPCAM*, and other EMT signature genes, such as *Claudins*, at d11/12 was rescued by d21 (Figure S3D), and KO cells differentiated into EPCAM^{high}-expressing tubule cells, although with reduced efficiency (Figure S2C). Importantly, formation of EPCAM^{high} cells was impaired not only in KO^{iPSC} and KO^{d4-7} but also in KO^{d11-14} organoids, in which exit from the NPC state and EPCAM^{mid} regulation was unperturbed. Tubular differentiation defects in KO organoids are therefore due to WT1's role in epithelial maturation rather than its earlier function in activating MET. Notably, epithelial elements are also found in WT with *WT1* lesions (Schumacher et al., 1997), and *WT1* mutations can be detected in epithelial cells of patient-derived organoids (Calandrini et al., 2020).

In addition to perturbing kidney development, early loss of *WT1* causes upregulation of muscle genes both in mouse (Berry et al., 2015) and in human kidney organoids. This indicates a conserved role of WT1 in repressing competing paraxial mesoderm fates, and suggests that expression of myogenic genes in a subset of WT patients (Gadd et al, 2012, 2017; Miyagawa et al., 1998) reflects the developmental history rather than plasticity of the tumors (Shukrun et al., 2014).

In mouse, constitutive *WT1* deletion causes apoptosis of the metanephric mesenchyme (Kreidberg et al., 1993), while NPC induction is largely unperturbed in KO^{iPSC} and KO^{d4-7} organoids (Figure S3B). Although this difference may be because of species-specific *WT1* functions or because of non-cell-autonomous rescue in organoids by unrecombined wild-type cells, we speculate that *in vitro* culture conditions compensate for *WT1* deficiency: Deletion of *FGF receptor 1* (*Fgfr1*) and *Fgfr2*, and of *Fgf20* and *Fgf9* in mice causes phenotypes that are reminiscent of loss of *WT1* (Barak et al., 2012; Poladia et al., 2006). WT1 directly binds to and regulates the transcription of several *Fgf* genes, and treatment of *WT1* mutant embryonic kidneys with recombinant FGF20 rescues cell death (Motamedi et al., 2014). The extrinsic FGF9 that is added between d7 and d14 of organoid formation may therefore suppress the pro-apoptotic effect of *WT1* loss and expose WT1's oncogenic role in developmentally more advanced NPCs.

Passaging in organoids showed that wild-type cells provide niche signals that maintain proliferation and expansion of mutant SIX2^{pos} cells in the presence of differentiation-promoting cues. In particular, we were not able to propagate mutant SIX2^{pos} cells in isolation. Future studies will be required to dissect how cell-to-cell contact, secreted signals, and spatial organization establish a growth-permissive environment. It is conceivable that *WT1* ablation in developing organoids resembles cancer initiation in an intact tissue context, while cell mixing recapitulates subsequent aspects of tumor growth in patients. We note that primary WT biopsies can be repeatedly passaged as spheroids (Wegert et al., 2020) and organoids (Calandrini et al., 2020) in three dimensions. Although growth conditions differ, it is possible that *WT1* KO kidney organoids recapitulate early stages of the disease, and that further tumor progression leads to independence of niche signals.

Taken together, we here establish a human kidney organoid-based tumorigenesis model by inducible deletion of *WT1*, complementing the current toolbox of pre-clinical WT models. We show that WT1 drives exit from the human

NPC state and, consequentially, prevents NPC hyperplasia, and that loss of *WT1* recapitulates defects observed in a clinically relevant patient subset. Overall, our work motivates the use of human kidney organoids to study pediatric kidney tumorigenesis. Tumor organoids provide access to the cancer cell type of origin, to crosstalk between different oncogenes and tumor suppressors, to interactions with the niche environment, and, eventually, to organotypic and phenotypic platforms for drug discovery and development.

EXPERIMENTAL PROCEDURES

Kidney organoids

iPSCs were differentiated into NPCs for 9 days on Laminin (Biolamina #LN521)-coated six-well-plates and, after single cell-dissociation using TrypLE Express (Thermo Fisher #12604013), transferred into ultra-low-attachment 96-well plates (Thermo Fisher #174925) for organoid formation in suspension culture (Morizane et al., 2015; Ungricht et al., 2021). SIX2 and Cas9 were induced by adding 1 μg/mL and 0.2 μg/mL DOX (Clontech #631311), respectively. Chimeric organoids were generated by aggregating single-cell suspensions of *WT1* KO d21 organoids with GFP-expressing WT29-iCas9 d9 NPCs or with ruptured GFP-expressing WT29-iCas9 d21 organoids. See supplemental experimental procedures for details.

Flow cytometry

Single cells were fixed using the BD Cytofix/Cytoperm Fixation/Permeabilization Kit (BD Biosciences #554714) according to the manufacturer's instructions with the exception that 0.4% bovine albumin fraction V solution (Thermo Fisher #15260037) in PBS was added before centrifugation. Cells were incubated with primary antibodies in permeabilization buffer at 4°C for 60 min, washed three times, incubated with secondary antibodies at 4°C for 60 min, washed three times, and resuspended in permeabilization buffer. Flow cytometry was performed on a BD LSRFortessa or BD LRSII, and data analyzed using FlowJo software.

Immunofluorescence

Kidney organoids were washed with PBS twice and fixed with 4% paraformaldehyde in PBS for 20 min at 4°C. After washing three times with PBS, organoids were resuspended in 50% sucrose (Sigma #84097) in PBS and stored at 4°C. Organoids were embedded in a 7.5% gelatin solution (Millipore #48722 dissolved in 10% sucrose in PBS) overnight at 4°C and mounted with Q Path Tissue OCT Medium (VWR #0011243) to generate frozen blocks that were cut into 10–14-μm sections using a Leica CM3050S cryostat. Sections were stained (see supplemental experimental procedures), images acquired on Zeiss LSM710 and LSM900 scanning head confocal microscopes, and processed with Fiji software.

Data availability

The accession number for the RNA-seq data reported in this study is ArrayExpress : E-MTAB-9957.

SUPPLEMENTAL INFORMATION

Supplemental information can be found online at https://doi.org/10.1016/j.stemcr.2021.07.023.

AUTHOR CONTRIBUTIONS

V.W., R.U., P.S.H., and J.B. conceived the study. V.W. designed and performed all experiments and analyzed the data. R.U. adapted the organoid protocol, generated the WT29-iCas9 and GFP-expressing WT29-iCas9 lines, and performed CDH1 staining of *WT1* KO organoids. J.B. performed computational analyses. J.B. and P.S.H. supervised the study. V.W. and J.B. wrote the manuscript with input from all authors.

CONFLICTS OF INTEREST

The authors declare no competing interests.

ACKNOWLEDGMENTS

S.A. Smallwood and team (FMI) for library preparation and sequencing; P. Papasaikas and M.B. Stadler (FMI) for help with computational analysis; L. Gelman (FMI) for help with confocal microscopy; M. Rittirsch for technical assistance; L. Morelli (Novartis) for help with virus production and infection; M. Mueller (Novartis) for providing the WT29 iPSC line; and H. Grosshans, S. Gasser (FMI), and S. Lienkamp (University of Zurich) for comments on the manuscript. V.W. acknowledges support by a Boehringer Ingelheim Fonds PhD fellowship, and J.B. from the Novartis Research Foundation.

Received: February 18, 2021
Revised: July 30, 2021
Accepted: July 30, 2021
Published: August 26, 2021

REFERENCES

Barak, H., Huh, S.-H., Chen, S., Jeanpierre, C., Martinovic, J., Parisot, M., Bole-Feysot, C., Nitschké, P., Salomon, R., Antignac, C., et al. (2012). FGF9 and FGF20 maintain the Stemness of nephron progenitors in mice and man. Dev. Cell *22*, 1191–1207.

Berry, R.L., Ozdemir, D.D., Aronow, B., Lindström, N.O., Dudnakova, T., Thornburn, A., Perry, P., Baldock, R., Armit, C., Joshi, A., et al. (2015). Deducing the stage of origin of Wilms' tumours from a developmental series of Wt1-mutant mice. Dis. Model Mech. *8*, 903–917.

Calandrini, C., Schutgens, F., Oka, R., Margaritis, T., Candelli, T., Mathijsen, L., Ammerlaan, C., van Ineveld, R.L., Derakhshan, S., de Haan, S., et al. (2020). An organoid biobank for childhood kidney cancers that captures disease and tissue heterogeneity. Nat. Commun. *11*, 1310.

Clevers, H., and Tuveson, D.A. (2019). Organoid models for cancer research. Annu. Rev. Cancer Biol *3*, 223–234.

Creighton, C.J., Morgan, M., Gunaratne, P.H., Wheeler, D.A., Gibbs, R.A., Robertson, A.G., Chu, A., Beroukhim, R., Cibulskis, K., Signoretti, S., et al. (2013). Comprehensive molecular characterization of clear cell renal cell carcinoma. Nature *499*, 43–49.

Davis, C.F., Ricketts, C.J., Wang, M., Yang, L., Cherniack, A.D., Shen, H., Buhay, C., Kang, H., Kim, S.C., Fahey, C.C., et al. (2014). The somatic genomic landscape of chromophobe renal cell carcinoma. Cancer Cell *26*, 319–330.

Gadd, S., Huff, V., Huang, C.-C., Ruteshouser, E.C., Dome, J.S., Grundy, P.E., Breslow, N., Jennings, L., Green, D.M., Beckwith, J.B., et al. (2012). Clinically relevant subsets identified by gene expression patterns support a revised ontogenic model of Wilms tumor: a Children's Oncology Group study. Neoplasia *14*, 742–756.

Gadd, S., Huff, V., Walz, A.L., Ooms, A.H.A.G., Armstrong, A.E., Gerhard, D.S., Smith, M.A., Auvil, J.M.G., Meerzaman, D., Chen, Q.-R., et al. (2017). A Children's Oncology Group and TARGET initiative exploring the genetic landscape of Wilms tumor. Nat. Genet. *49*, 1487–1494.

Hanahan, D., and Coussens, L.M. (2012). Accessories to the crime: functions of cells recruited to the tumor microenvironment. Cancer Cell *21*, 309–322.

Hastie, N.D. (2017). Wilms' tumour 1 (WT1) in development, homeostasis and disease. Development *144*, 2862–2872.

Hochane, M., van den Berg, P.R., Fan, X., Bérenger-Currias, N., Adegeest, E., Bialecka, M., Nieveen, M., Menschaart, M., Chuva de Sousa Lopes, S.M., and Semrau, S. (2019). Single-cell transcriptomics reveals gene expression dynamics of human fetal kidney development. PLoS Biol. *17*, e3000152.

Huang, L., Mokkapati, S., Hu, Q., Ruteshouser, E.C., Hicks, M.J., and Huff, V. (2016). Nephron progenitor but not stromal progenitor cells give rise to Wilms tumors in mouse models with β-catenin activation or Wt1 ablation and Igf2 upregulation. Neoplasia *18*, 71–81.

Hynds, R.E., Vladimirou, E., and Janes, Sam.M. (2018). The secret lives of cancer cell lines. Dis. Model Mech. *11*, dmm037366.

Kann, M., Ettou, S., Jung, Y.L., Lenz, M.O., Taglienti, M.E., Park, P.J., Schermer, B., Benzing, T., and Kreidberg, J.A. (2015). Genome-wide analysis of Wilms' tumor 1-controlled gene expression in podocytes reveals key regulatory mechanisms. J. Am. Soc. Nephrol. *26*, 2097–2104.

Kersten, K., de Visser, K.E., van Miltenburg, M.H., and Jonkers, J. (2017). Genetically engineered mouse models in oncology research and cancer medicine. Embo Mol. Med. *9*, 137–153.

Kreidberg, J.A., Sariola, H., Loring, J.M., Maeda, M., Pelletier, J., Housman, D., and Jaenisch, R. (1993). WT-1 is required for early kidney development. Cell *74*, 679–691.

Lindström, N.O., Brandine, G.D.S., Tran, T., Ransick, A., Suh, G., Guo, J., Kim, A.D., Parvez, R.K., Ruffins, S.W., Rutledge, E.A., et al. (2018). Progressive recruitment of mesenchymal progenitors reveals a time-dependent process of cell fate acquisition in mouse and human nephrogenesis. Dev. Cell *45*, 651–660, e4.

Miyagawa, K., Kent, J., Moore, A., Charlieu, J.-P., Little, M.H., Williamson, K.A., Kelsey, A., Brown, K.W., Hassam, S., Briner, J., et al. (1998). Loss of WT1 function leads to ectopic myogenesis in Wilms' tumour. Nat. Genet. *18*, 15–17.

Morizane, R., Lam, A.Q., Freedman, B.S., Kishi, S., Valerius, M.T., and Bonventre, J.V. (2015). Nephron organoids derived from human pluripotent stem cells model kidney development and injury. Nat. Biotechnol. *33*, 1193–1200.

Motamedi, F.J., Badro, D.A., Clarkson, M., Lecca, M.R., Bradford, S.T., Buske, F.A., Saar, K., Hübner, N., Brändli, A.W., and Schedl, A. (2014). WT1 controls antagonistic FGF and BMP-pSMAD pathways in early renal progenitors. Nat. Commun. *5*, 4444.

Network, C.G.A.R., Linehan, W.M., Spellman, P.T., Ricketts, C.J., Creighton, C.J., Fei, S.S., Davis, C., Wheeler, D.A., Murray, B.A., Schmidt, L., et al. (2016). Comprehensive molecular characterization of papillary renal-cell carcinoma. N. Engl. J. Med. *374*, 135–145.

Pode-Shakked, N., Gershon, R., Tam, G., Omer, D., Gnatek, Y., Kanter, I., Oriel, S., Katz, G., Harari-Steinberg, O., Kalisky, T., et al. (2017). Evidence of in vitro preservation of human nephrogenesis at the single-cell level. Stem Cell Reports *9*, 279–291.

Poladia, D.P., Kish, K., Kutay, B., Hains, D., Kegg, H., Zhao, H., and Bates, C.M. (2006). Role of fibroblast growth factor receptors 1 and 2 in the metanephric mesenchyme. Dev. Biol. *291*, 325–339.

Schumacher, V., Schneider, S., Figge, A., Wildhardt, G., Harms, D., Schmidt, D., Weirich, A., Ludwig, R., and Royer-Pokora, B. (1997). Correlation of germ-line mutations and two-hit inactivation of the WT1 gene with Wilms tumors of stromal–predominant histology. Proc. Natl. Acad. Sci. U S A *94*, 3972–3977.

Shukrun, R., Pode-Shakked, N., Pleniceanu, O., Omer, D., Vax, E., Peer, E., Pri-Chen, S., Jacob, J., Hu, Q., Harari-Steinberg, O., et al. (2014). Wilms' tumor blastemal stem cells dedifferentiate to propagate the tumor bulk. Stem Cell Reports *3*, 24–33.

Treger, T.D., Chowdhury, T., Pritchard-Jones, K., and Behjati, S. (2019). The genetic changes of Wilms tumour. Nat. Rev. Nephrol. *15*, 240–251.

Ungricht, R., Guibbal, L., Lasbennes, M.-C., Orsini, V., Beibel, M., Waldt, A., Cuttat, R., Carbone, W., Basler, A., Roma, G., et al. (2021). Genome-wide screening in human kidney organoids identifies novel aspects of nephrogenesis. bioRxiv https://doi.org/10.1101/2021.05.26.445745.

Wegert, J., Zauter, L., Appenzeller, S., Otto, C., Bausenwein, S., Vokuhl, C., Ernestus, K., Furtwängler, R., Graf, N., and Gessler, M. (2020). High-risk blastemal Wilms tumor can be modeled by 3D spheroid cultures in vitro. Oncogene *39*, 849–861.

Stem Cell Reports, Volume *16*

Supplemental Information

The tumor suppressor WT1 drives progenitor cell progression and epithelialization to prevent Wilms tumorigenesis in human kidney organoids

Verena Waehle, Rosemarie Ungricht, Philipp S. Hoppe, and Joerg Betschinger

Waehle et al., Supplemental Figure 1

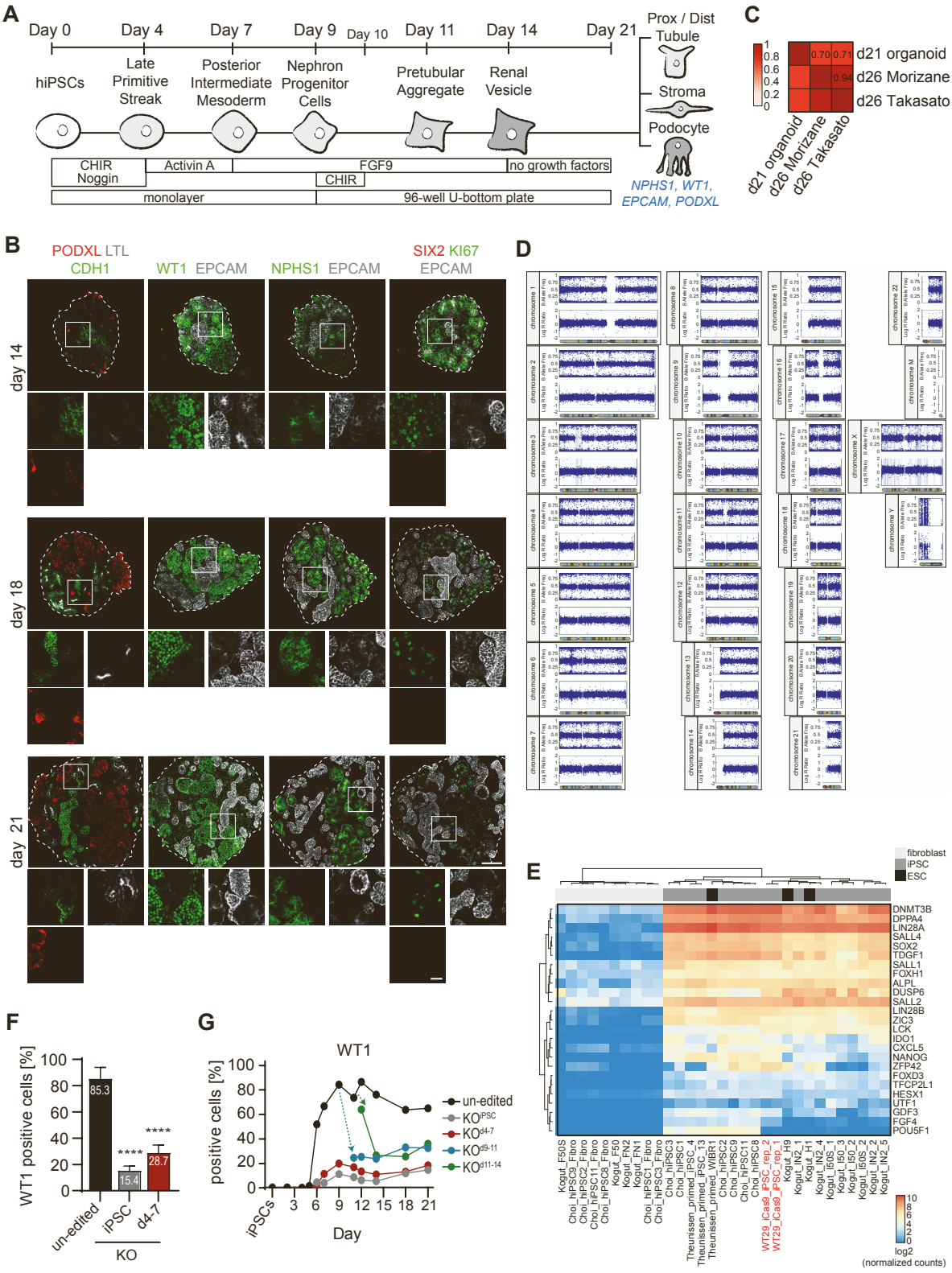

Figure S1: Related to Figure 1

A: Overview of the kidney organoid protocol adapted from (Morizane et al., 2015); Prox = proximal; Dist = distal; CHIR = CHIR99021.

B: Staining of the indicated markers in representative d14, d18 and d21 organoids (Scale bar: 100 µm). White boxed regions are shown as blow-ups (Scale bar: 25 µm).

C: Pearson correlation coefficients of pairwise comparisons between Log2 fold gene expression changes of indicated organoid samples relative to corresponding iPSC samples. Expression data for d26, Morizane and d26, Takasato are from (Wu et al., 2018), and the mean of 4 and 6 technical and biological replicates, respectively.

D: Karyogram of WT29-iCas9 iPSCs. Mean log R ratio (LRR) and B-allele frequency (BAF) are shown. Freq = Frequency

E: Unsupervised clustering of pluripotency marker gene expression in fibroblasts, human embryonic stem cells (ESCs) and iPSCs across different studies. The WT29-iCas9 iPSCs used in this work are highlighted in red.

F: Quantification of WT1-expressing cells in un-edited, KO^{iPSC} and KO^{d4-7} d9 NPCs by flow cytometry. Data presented as mean % of positive cells +/- SD from n=7 independent experiments.

G: Quantification of WT1-expressing cells by flow cytometry in un-edited, KO^{iPSC}, KO^{d4-7}, KO^{d9-11} cells and KO^{d11-14} organoids at the indicated time points, or in iPSCs (un-edited or KO^{iPSC}). Data is presented from one experiment. Arrows visualize reduction of WT1 protein expression upon induction of Cas9 from d9-11 and d11-14.

Waehle et al., Supplemental Figure 2

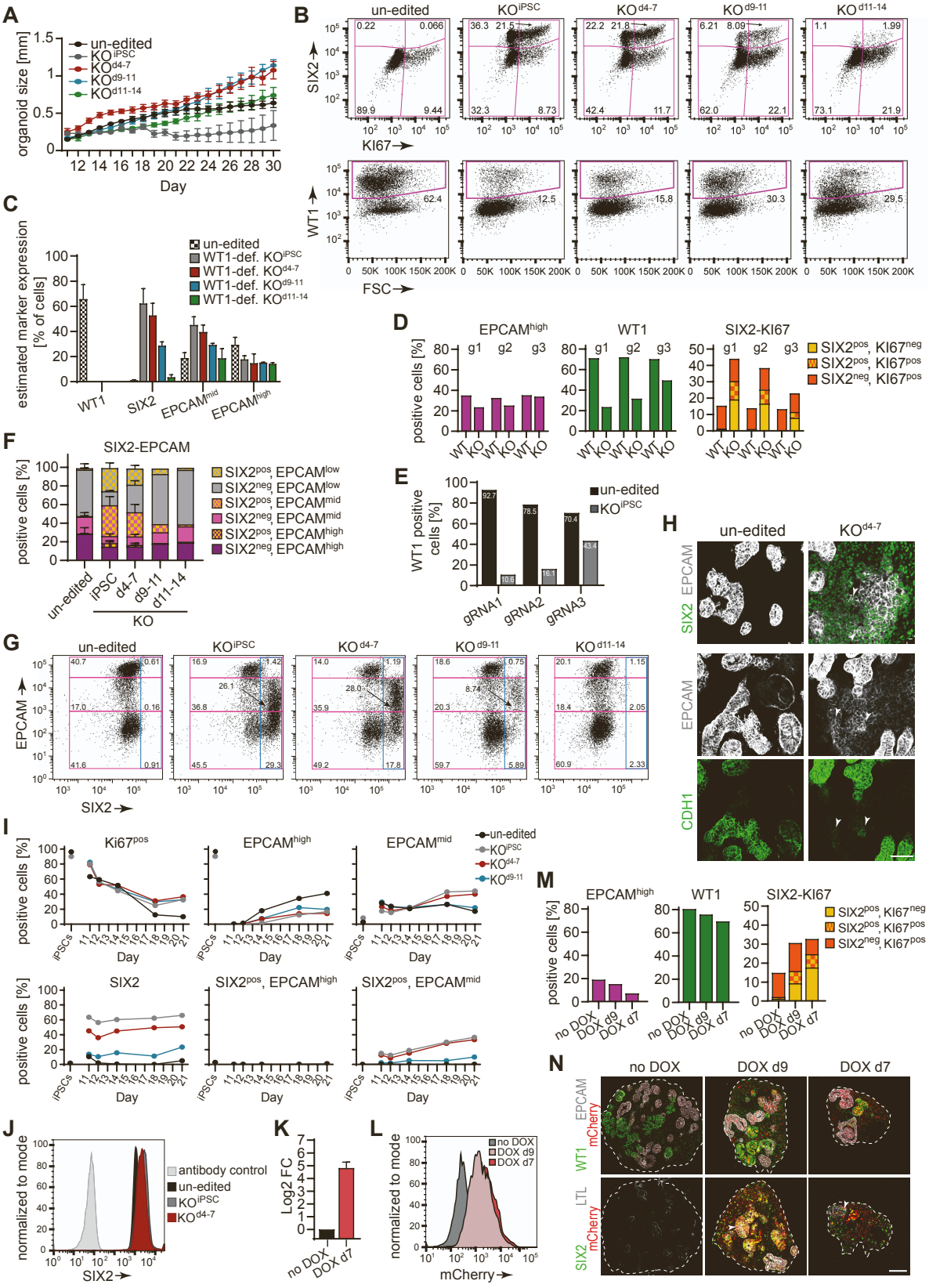

Figure S2: Related to Figure 1.

A: Growth of un-edited, KO^{iPSC}, KO^{d4-7}, KO^{d9-11} and KO^{d11-14} organoids between d11 and d30. Areas were derived from Incucyte® images and are presented as mean +/- SD for a minimum of n=10 organoids across all time points.

B: Representative flow cytometry dot plots showing SIX2 and KI67 staining (top) and WT1 staining (bottom) in d21 organoids as in **A**, and used for quantifications shown in **Figure 1A**. Pink boxes represent gates used for quantification and numbers indicate % of cells in the respective gates.

C: To gauge the cell type distribution of WT1-deficient and WT1-expressing cells in KO organoids, we estimated the percentage of WT1-deficient cells that express the indicated markers in KO^{iPSC}, KO^{d4-7}, KO^{d9-11} and KO^{d11-14} d21 organoids (see Supplemental Experimental Procedures) . Data is presented as estimated mean % of positive cells +/- SD in n=5 (un-edited, KO^{iPSC}, KO^{d4-7}) or n=2 (KO^{d9-11}, KO^{d11-14}) independent experiments. Values for un-edited d21 organoids are shown for reference and were taken from **Figure 1A,C**. WT1-def. = WT1-deficient cells

D: Quantification of subpopulations by flow cytometry of indicated markers in un-edited or KO^{iPSC} d21 organoids using indicated *WT1* gRNAs (g1, g2, g3). Data is presented from one experiment.

E: Quantification by flow cytometry of WT1-expressing cells in un-edited and KO^{iPSC} d9 NPCs using indicated *WT1* gRNAs. Data presented from one experiment.

F: Quantification of subpopulations by flow cytometry of indicated markers in d21 organoids as in **A**. Data is presented as mean % of positive cells +/- SD derived from n=5 (un-edited, KO^{iPSC}, KO^{d4-7}) and n=1 (KO^{d9-11}, KO^{d11-14}) independent experiments. Note that the SIX2-EPCAM quantification includes data presented in the d21 panel of **Figure 1C**. Two-sided student's t-test; *p*-value: ns >0.05; * ≤0.05; ** ≤0.01; *** ≤0.001; **** ≤0.0001.

G: Representative flow cytometry dot plots showing EPCAM and SIX2 staining in d21 organoids as in **A**. Pink boxes and associated numbers indicate % of cells that are $EPCAM^{high}$, $EPCAM^{mid}$ and $EPCAM^{low}$. Blue boxes and associated numbers indicate % of cells that are $SIX2^{pos}/EPCAM^{high}$, $SIX2^{pos}/EPCAM^{mid}$ or $SIX2^{pos}/EPCAM^{low}$.

H: Staining of indicated markers in representative un-edited and KO^{d4-7} d21 organoids. Images were enhanced to visualize EPCAM staining surrounding SIX2-positive cells (top) as well as overlap of EPCAM (middle) and CDH1 staining (bottom) in KO^{d4-7} organoids (white arrowheads). Note that images of SIX2-EPCAM staining are blow-ups derived from respective images in **Figure 1B**. Scale bar: 200 µm.

I: Quantification of subpopulations by flow cytometry of indicated markers in un-edited, KO^{iPSC}, KO^{d4-7} and KO^{d9-11} organoids at the indicated time points, or in iPSCs (un-edited or KO^{iPSC}). Data is presented from one experiment.

J: SIX2 expression in d9 NPCs by flow-cytometry.

K: qPCR analysis of *SIX2* transcription in d9 NPCs derived from mCherry::T2A::SIX2 iPSCs that were untreated (no DOX) or treated with DOX from d7 onwards. Data is presented as Log2 fold expression change relative to the untreated control, and shown as mean +/- SD derived from n=3 experiments.

L: mCherry expression in d21 organoids that were untreated (no DOX) or treated with DOX starting from the indicated time points to induce mCherry::T2A::SIX2 expression.

M: Quantification by flow cytometry of subpopulations expressing indicated markers in d21 organoids that were untreated (no DOX) or treated with DOX as in **L**. Data is shown as % of positive cells for one representative experiment.

N: Staining of indicated markers in representative d21 organoids that were untreated (no DOX) or treated with DOX as in **L**. mCherry represents induction of SIX2. White arrowheads indicate expression of SIX2 in LTL^{pos} tubules. Scale bar: 100 µm.

Waehle et al., Supplemental Figure 3

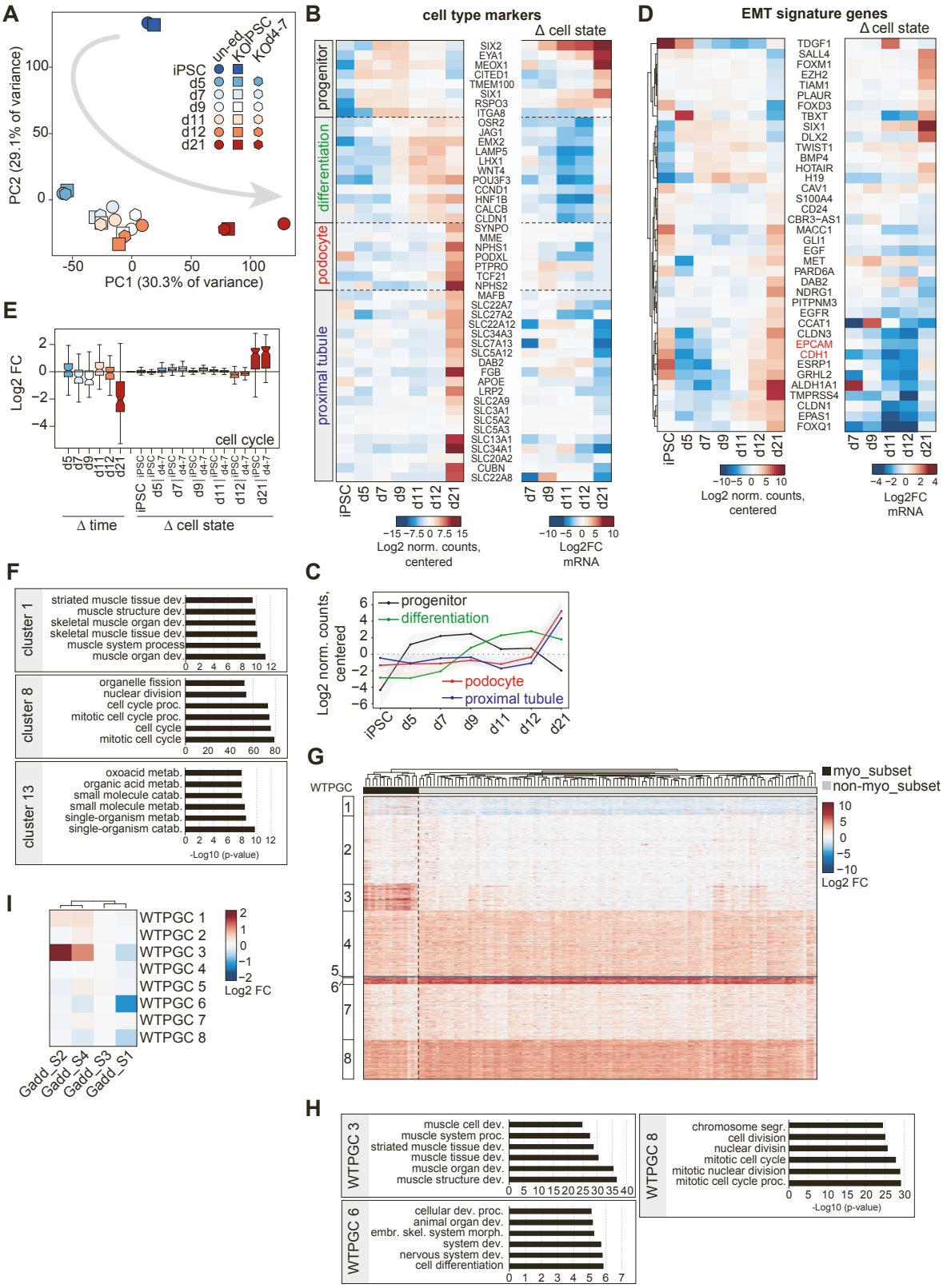

Figure S3: Related to Figures 2 and 3.

A: Principal component (PC) analysis of un-edited (un-ed.), KO^{iPSC} and $KO^{d4\text{-}7}$ samples at the indicated time points.

B: Heatmap of marker gene expression changes during organoid development (left) and in KO organoids (right). Note that Log2 fold changes relative to the mean in un-edited organoids at indicated time points (left) and Log2 fold changes of mean expression changes in KO^{iPSC} and $KO^{d4\text{-}7}$ organoids relative to un-edited control organoids at indicated time points (right) are shown. Cell types are indicated on the left.

C: Line representation of marker gene expression changes shown in **B**. Lines represent the medium and shades the lower and upper quartile.

D: Heatmap of gene expression changes of selected (see Supplemental Experimental Procedures) EMT marker genes as in **B**.

E: Quantification of Log2 fold expression changes of cell cycle genes and of contrasts as specified in **Figure 2A**. The cell cycle gene-set include G_1S- and G_2M-specific gene-sets (Liu et al., 2017).

F,H: The top six GO terms that are enriched in each of the indicated gene clusters is shown. catab. = catabolism; dev. = development; embr. = embryonic; metab. = metabolism; morph. = morphogenesis; proc. = process; segr. = segregation; skel. = skeletal.

G: k-means clustering of scaled Log2 fold expression changes in WT patients relative to control tissue of 2,100 genes (see Supplemental Experimental Procedures). Unsupervised clustering of patients identified a myogenic subset (myo_subset) in which Wilms tumor patient gene cluster (WTPGC) 3 is strongly induced.

I: Heatmap representation of mean-centered scaled Log2 fold expression changes of WTPGCs 1-8 in patient subsets defined by (Gadd et al., 2012).

Waehle et al., Supplemental Figure 4

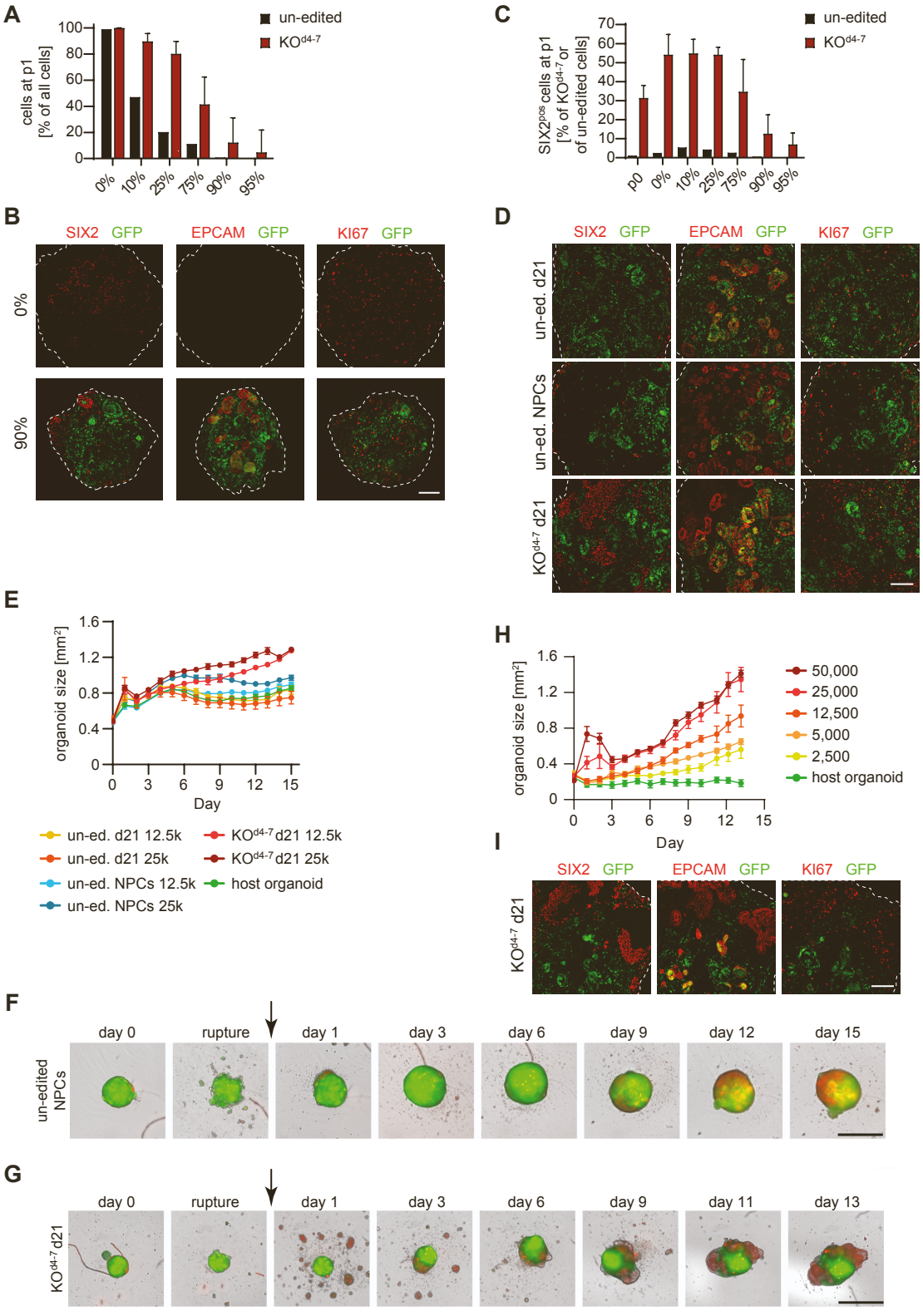

Figure S4: Related to Figure 4.

A,**C:** Quantification of, **A** all, and **C** SIX2^{pos} un-edited and KO^{d4-7} cells in chimeric organoids after passaging in the presence of wild-type GFP-expressing d9 NPCs at indicated ratios after passage 1. p0 indicates KO^{d4-7} d21 organoids that were used as starting material for passaging. Data is shown as mean % +/- SD for n=2 independent experiments. **A**: Percentages are relative to all cells of chimeric organoids (% of all cells). **C**: Percentages are relative to all mutant cells (% of KO^{d4-7} cells), and relative to all un-edited control cells (% of un-edited cells). In both cases, the GFP-expressing cells are excluded from the analysis.

B,**D**,**I:** Staining of the indicated markers, **B** at passage 3 and indicated mixing ratios, **D** 15 d after adding 12,500 RFP-expressing cells from un-edited d21 organoids (un-ed. d21, top), un-edited d9 NPCs (un-ed. NPCs, middle), or KO^{d4-7} d21 organoids (KO^{d4-7} d21, bottom) to ruptured wild-type GFP-expressing organoids in the presence of FGF9/CHIR, and **I** after adding 12,500 RFP-expressing cells from KO^{d4-7} d21 organoids to ruptured wild-type GFP-expressing organoids in the absence of growth factors. Scale bar: 100 µm.

E,**H:** Growth of organoids, **E** after adding 12,500 (12.5k) or 25,000 (25k) RFP-expressing cells to ruptured wild-type GFP organoids in the presence of FGF9/CHIR as specified in **D**, and **H** after adding the indicated numbers of RFP-expressing KO^{d4-7} d21 organoid cells to ruptured wild-type GFP organoids in the absence of growth factors. Areas were calculated from Incucyte® images and are presented as mean +/- standard error of the mean (SEM) for n=8 organoids per condition.

F,**G:** Images of organoids obtained after adding, **F** 12,500 RFP-expressing un-edited d9 NPCs to ruptured wild-type GFP organoids in the presence of FGF9/CHIR, and **G** 12,500 RFP-expressing cells from KO^{d4-7} d21 organoids to ruptured wild-type GFP organoids in the absence of growth factors. Images were recorded at the indicated time points using an Incucyte® system. Scale bar 1 mm.

SUPPLEMENTAL EXPERIMENTAL PROCEDURES

Human iPSC culture

WT29 and WT29-iCas9 iPSCs (Ungricht et al., 2021) and their derivatives were cultured on Laminin (Biolaminin 521 LN; Biolamina #LN521) in mTeSR1 (Stem Cell Technologies; # 85850) plus 1% Penicillin-Streptomycin (Thermo Fisher #15140122). For passaging, cells were detached using TrypLE Express (Thermo Fisher #12604013), and single-cell suspensions were plated in mTeSR1 supplemented with 2 µM ROCK inhibitor (Y-27632 Dihydrochloride Tocris #1254).

Karyotyping

Using the service of Life&Brain Genomics (https://www.lifeandbrain.com/en/products-services/lb-genomics/), genomic DNA of WT29-iCas9 iPSCs was hybridized to the HumanOmni_EUR_HD_20021594_BeadChip array (Illumina), scanned on an Illumina iScan and analyzed using GenomeStudio V2.0.2 and CNV-Partition. The Karyogram is provided in Figure S1D.

Kidney organoid protocol

Adherent differentiation (d0-d9): 50'000-60'000 hiPSCs/cm^2 were plated in mTeSR1 supplemented with 2 µM ROCK inhibitor into Laminin-coated 6-well plates. After at least 6 h, medium was removed, cells gently washed with Dulbecco's Phosphate Buffered Saline (PBS; without magnesium and calcium; Thermo Fisher #14190169), and differentiation induced by adding basic differentiation medium (BDM; advanced RPMI 1640 (Thermo Fisher #12633012), 1% Glutamax (Thermo Fisher #35050038), 1% Penicillin-Streptomycin) supplemented with 8 µM CHIR99021 (Tocris #4423) and 5 ng/ml Noggin (Peprotech #120-10C) (= d0). Medium was changed after 2d. At d4, cells were visually inspected for the presence of contracting colonies with bright halo-like outlines, followed by a medium change to BDM containing 10 ng/ml Activin A (R&D Systems #338_AC). At d7, medium was changed to BDM supplemented with 10 ng/ml FGF9 (R&D Systems #273-F9). At d9, corresponding to the NPC state, cells were washed, dissociated from the cell culture dish using TrypLE and counted using a Vi-CELL™ XR Cell Viability Analyzer (Beckmann).

Organoid differentiation in suspension culture (d9 onwards): 25'000 or 50'000 cells were seeded in 150 µl of BDM containing 3 µM CHIR99021, 10 ng/ml FGF9 and 2 µM ROCK inhibitor into Corning® Costar® Ultra-Low Attachment 96-well round bottom plates (Sigma #CLS7007-24EA). Surplus NPCs were frozen in CryoStor® CS10 (Stem Cell Technologies #7930). To induce aggregation, the plate was briefly centrifuged at 90 g for 3 minutes (min). At d10 (d1 in suspension), 100 µl of medium was replaced with 150 µl of BDM plus 10 ng/ml FGF9. At d11 (d2), 100 µl of medium was replaced with 100 µl of BDM plus 10 ng/ml FGF9. At d14 (d5), d16 (d7) and d18 (d9), 100 µl of medium was replaced with 100 µl of BDM without growth factors. During culture beyond d21, medium was changed 3 times per week.

Throughout the study we compared the mutant edited organoids with wild-type un-edited control organoids that were generated side-by-side and analyzed at the same differentiation time points.

Organoid growth was determined using an Incucyte® system: Brightfield images were recorded every 24h, or as indicated, and organoid sizes were calculated. Object recognition parameters were manually defined for each experiment, and the detected objects validated.

Generation of single cell suspensions for flow cytometry or passaging of organoids

To generate single cell suspensions for flow cytometry or passaging, organoids were transferred into tubes using a cut P-1000 tip, and washed twice with PBS. A 1:1 mix of non-enzymatic cell dissociation solution (Thermo Fisher #13151014) and 0.25% Trypsin-EDTA (Thermo Fisher #25200056) was added for 10 mins at 37°C, and organoids were dissociated by pipetting up and down ten times. Trypsin was inactivated by adding 10% fetal calf serum (FCS; Bioconcept #2-01F36-I) in PBS, washed with 1% FCS and passed through a 50 µm filter (BD Biosciences #340632).

Generation and culture of chimeric organoids

For mixing with NPCs (Figure 4B,C, S4A-C), single cell suspensions of RFP-expressing un-edited or KO^{d4-7} d21 organoids were generated as described above, aggregated with freshly thawed GFP-expressing WT29-iCas9 (Ungricht et al., 2021) d9 NPCs at indicated ratios to a total of 50,000 cells, and plated into Ultra-Low Attachment 96-well round bottom plates in 150 µl BDM, supplemented with 3 µM CHIR99021, 10 ng/ml FGF9 and 2 µM ROCK inhibitor. Culture was continued as detailed in «Organoid differentiation in suspension culture» above. At d12 of suspension culture, organoids were dissociated into single cell suspensions that were used for flow cytometry analysis and for passaging by aggregating with freshly thawed GFP-expressing WT29-iCas9 d9 NPCs at respective ratios and subjecting to suspension culture. This was repeated for up to four passages. After each passage, a minimum of six organoids was processed for cryosectioning and immunofluorescence staining, as described below.

For mixing into d21 organoids (Figure 4D, S4E-I), GFP-expressing WT29-iCas9 d21 organoids were mechanically ruptured by pipetting them up and down five times in a P-200 tip. RFP-expressing un-edited and KO^{d4-7} d21 organoids were dissociated into single cell suspensions as described above, and un-edited RFP-expressing d9 NPCs were freshly thawed. After cell counting, indicated cell numbers were added to ruptured organoids, plates briefly spun to induce aggregation, and culture in BDM resumed as indicated, either in the presence or absence of 3 µM CHIR99021 and 10 ng/ml FGF9 according to «Organoid differentiation in suspension culture» above.

Molecular biology

The coding sequence of SIX2 was amplified from human iPSC cDNA, T2A sequences and Gateway cloning sites added by polymerase chain reaction (PCR), and recombined into pDONR221 using Gateway technology (Thermo Fisher #11789020 and #11791020). The expression vector was generated by recombining with a PiggyBac pPB-TRE-mCherry-DEST-rTA-HSV-neo expression destination vector. *WT1* gRNA-encoding vectors are derived from pRSI16-U6-sh-UbiC-TagRFP-2A-Puro (Cellecta #SVSHU616-L).

Oligonucleotide sequences:

SIX2 (gateway)	attB1-fwd	ggggacaagtttgtacaaaaaagcaggcttcaccATGTCCATGCTGCCCACCTTCG
	attB2-rev	ggggaccactttgtacaagaaagctgggtcCTAGGAGCCCAGGTCCACGAGG
T2A sequence	fwd	GAGGGCAGAGGAAGTCTCCTAACATGCGGTGACGTGGAGGAGAATCCTGGCCCA

fwd = forward sequence; rev = reverse sequence

gRNA sequences:

WT1	#1	TGTGTTTGCAGCCACAGCAC
WT1	#2	GGTGTGGCAGCCATAGACCG
WT1	#3	GCTGCCGGTGCAGCTGTCGG

Generation of transgenic WT29 iPSCs for SIX2 overexpression

Transgenic WT29 iPSCs were generated by transfecting PiggyBac expression vector and pBase (Villegas et al., 2019) using Lipofectamin Stem™ (Thermo Fisher #STEM00015) in OptiMem Reduced Serum Medium (Thermo Fisher #319850629), and selected for stable integration in the presence of 100 µg/ml G418 (Thermo Fisher #10131027). Inducible cells were further selected by exposing to 1 µg/ml Doxycycline (DOX; Clonetech #631311) for 48 h and purifying the 30% of cells with mCherry expression closest to the median of the population. Cell sorting was performed on a BD FACSAria™ Fusion Cell Sorter.

Lentivirus production and human iPSC *transduction*

Lentiviruses were produced in HEK293T cells. Prior to transfection, HEK293T cells were seeded onto collagen I-coated 6-well tissue culture plates (BD biosciences #346400) in packaging medium (DMEM (Thermo Fisher #11965), supplemented with 10% FCS and 1% Non-essential amino acids (Thermo Fisher #11140050)). The next day, cells were transfected with *WT1* gRNA-encoding vectors and Cellecta packaging mix (Cellecta #CPC-K2A) using the TransIT™293 transfection reagent (Mirus Bio #MIR 2700) in OptiMem Reduced Serum Medium (Thermo Fisher #31985062). The next day, medium was changed to 1 ml of packaging medium. After 3d, the virus-containing supernatant was collected, filtered through a 50 µm filter and stored at -80°C.

For virus titration, WT29-iCas9 cells were seeded into 6-well plates (200,000 cells / well) in mTeSR1 medium supplemented with ROCK inhibitor. After 7 hours (h), different volumes of viral supernatant were added to the cells. After 3d with daily mTeSR1 medium changes, cells were detached and RFP fluorescence was measured by flow cytometry. Based on this titration, WT29-iCas9 cells were transduced at a multiplicity of infection of 0.5, and infected cells were selected with puromycin (Thermo Fisher #A11138-03) for 6d.

RNA isolation, cDNA synthesis, qPCR

RNA was isolated using RNeasy Mini Kits (Qiagen #74104) and RNase-Free-DNase Sets (Qiagen #79256) according to the manufacturer's instructions, and concentration determined using a NanoDrop (Thermo Fisher).

cDNA was generated from at least 400 ng of total RNA using SuperScript III Reverse Transcriptase (Thermo Fisher # 18080044) using oligodT priming. 25 ng of cDNA was subjected to qPCR on a Step One Plus™ Real-Time PCR System (Thermo Fisher) using the TaqMan Fast Universal PCR Master Mix (Thermo Fisher # 4364103). Expression of SIX2 was quantified in technical duplicates using Universal Probe Library (UPL, Roche) Probe 88 together with custom-designed primer pairs: Fwd: ggcaagtcggtgttaggc, Rev: ggctggatgatgagtggtct, and multiplexing with a *GAPDH* probe (Thermo Fisher # 4326317E) . Cycle threshold (CT) values were normalized to *GAPDH* and to controls (ΔΔCT method).

Flow cytometry of mCherry-expression

Single live cell suspensions were washed with 1% FCS in PBS and resuspended in flow cytometry buffer (2% FCS and 1 mM ethylenediaminetetraacetic acid (EDTA; Thermo Fisher #AM9260G) in PBS). Flow cytometry was performed on a BD LSRFortessa™ and data analyzed using FlowJo™ software.

Antibodies for flow cytometry of fixed cells

EPCAM-Alexa Fluor (AF) 647 (Abcam #ab239273, 1:200); KI67-FITC (eBisoscience #11-5698-82, 1:200); SIX2 (Proteintech #11562-1-AP, 1:100); WT1 (Abcam #ab89901, 1:200); donkey-anti-rabbit AF488 (Thermo Fisher #A-21206, 1:500); donkey-anti-rabbit AF 647 (Thermo Fisher #A-31573, 1:500).

Estimating RFP expression in chimeric organoids

RFP-expression in fixed *WT1* KO cells of chimeric organoids (Figure 4B, S4A,B) by flow cytometry was ambiguous. We therefore determined the fraction of mutant cells in chimeric organoids by using opposing GFP-expression in wildtype cells. Heterogeneity of GFP expression was corrected for by comparing to the GFP distribution in GFP-expressing WT29-iCas9 host cells.

Immunofluorescence staining of Cryosections

Cryosections were washed with PBS for 10 mins at room temperature (RT). When using biotinylated LTL, slides were incubated with blocking/permeabilization buffer (1% BSA and 0.2% Triton X-100 in PBS) for 15 mins, then with blocking/permeabilization buffer containing four drops per ml of Streptavidin Block solution (Streptavidin/Biotin Blocking Kit; Vectorlabs #SP-2002) for 15 mins, and then with blocking/permeabilization buffer containing four drops per ml of Biotin Block solution for 15 mins. When using un-biotinylated primary antibodies, slides were instead incubated with blocking/permeabilization buffer for 30 mins at RT. After a quick wash in PBS, slides were incubated with primary antibodies in 1% BSA in PBS for 1 h at RT. Afterwards, slides were washed twice with PBS for each 10 mins, incubated with secondary antibodies and Hoechst 33342 diluted into 1% BSA in PBS for 1 h at RT, and after two additional washes with PBS for 10 mins each, mounted in ProLong™ Diamond Antifade Mountant (Thermo Fisher #P36970).

Antibodies were: CDH1 (BD Biosciences #610181, 1:200 and Thermo Fisher #MA514458, 1:100); EPCAM-AF647 (Abcam #ab239273, 1:200); Hoechst 33342 (Thermo Fisher #H3570; 1:10000); KI67 (SolA15, eBisoscience #14-5698-82, 1:200) (KI67 / KI67-FITC (SolA15, eBisoscience #14-5698-82, 1:200); LTL-Biotinylated (Vectorlabs B-1325, 1:500); NPHS1 (R&D Systems #AF4269, 1:60); PODXL (R&D Systems #AF1658, 1:500); SIX2 (Proteintech #11562-1-AP, 1:100); WT1 (Abcam #ab89901; 1:200); donkey-anti-rabbit AF 488 (Thermo Fisher #A-21206, 1:500); donkey-anti-rabbit AF 647 (Thermo Fisher #A-31573, 1:500); donkey-anti-goat AF 594 (Thermo Fisher #A-11058, 1:500); donkey-anti-goat AF 647 (Thermo Fisher #A-21447, 1:500); donkey-anti-sheep AF 488 (Thermo Fisher # A-11015, 1:500); donkey-anti-mouse AF 488 (Thermo Fisher #A-21202, 1:500); donkey-anti-rat AF 647 (Abcam #150155, 1:500); Streptavidin Fluorescent Dye 633-I (Abnova #U0295, 1:500).

Estimating the cell type distribution of WT1-deficient cells in KO organoids

In mosaic KO organoids, the observed percentage of cells expressing a particular cell type marker $\boldsymbol{p}_{marker}(mosaic\ organoid)$ equals $\boldsymbol{wt}_{marker} \cdot \boldsymbol{p}_{marker}(wildtype) + (1 - \boldsymbol{wt}_{marker}) \cdot \boldsymbol{p}_{marker}(KO)$, where $\boldsymbol{wt}_{marker}$ is the fraction of WT1-positive wild-type cells in mosaic organoids expressing this marker, and $\boldsymbol{p}_{marker}(wildtype \text{ or } KO)$ is the percentage of all wild-type or WT1-deficient (KO) cells in mosaic organoids expressing this marker.

To estimate $\boldsymbol{p}_{marker}(KO)$ (Figure S2C), we assume: (1) that $\boldsymbol{wt}_{marker}$ is invariable across cell types and equals the fraction of wild-type cells in podocytes defined by WT1 staining in mosaic and corresponding un-edited control organoids: $\boldsymbol{wt}_{marker} \approx \frac{\boldsymbol{p}_{WT1}\,(mosaic\ organoid)}{\boldsymbol{p}_{WT1}\,(unedited\ organoid)}$ (Figure 1A); and (2) that the propensity for differentiation towards a particular cell type is a cell-intrinsic

characteristic, such that $\boldsymbol{p}_{marker}(wildtype)$ equals the cell type distribution in un-edited control organoids: $\boldsymbol{p}_{marker}(wildtype) \approx \mathbf{p}_{\text{marker}}(\text{unedited organoid})$ (Figure 1A,C).

$$\boldsymbol{p}_{marker}(KO) \approx \frac{\boldsymbol{p}_{marker}(mosaic\ organoid) - \frac{\boldsymbol{p}_{WT1}(mosaic\ organoid)}{\boldsymbol{p}_{WT1}(unedited\ organoid)} \cdot \boldsymbol{p}_{marker}(unedited\ organoid)}{1 - \frac{\boldsymbol{p}_{WT1}(mosaic\ organoid)}{\boldsymbol{p}_{WT1}(unedited\ organoid)}}$$

Bioinformatics

RNA isolation of three independent biological replicates was performed as described above and RNA-seq libraries prepared using the TruSeq mRNA Library preparation kit (Illumina #20020595). RNA sequencing was performed on an Illumina HiSeq2500 machine (50 bp single-end reads). RNA-seq reads were aligned to the human hg38 genome using *qAlign* from the Bioconductor package QuasR (Gaidatzis et al., 2015) with default parameters except for *aligner="Rhisat2"* and *splicedAlignment=TRUE*. Alignments were quantified for known UCSC genes obtained from the TxDb.Hsapiens.UCSC.hg38.knownGene package using *qCount* (Table S1). Raw counts were further divided by the total number of counts in all genes in each sample , and multiplied with the minimum total counts across samples in order to normalize for different library sizes.

To evaluate selected pluripotent marker gene expression in pluripotent stem cells, the RNAseq data of the samples described in Figure S1E were downloaded from the datasets GSE82765 (Theunissen et al., 2016), GSE72311 (Choi et al., 2015) and GSE97265 (Kogut et al., 2018). Gene expression levels were determined as described above, normalized and Log2 transformed with a pseudocount of 1.

Principal component analysis (PCA) (Figure S3A) using normalized read counts of merged replicates and considering the top 30% variable genes was performed using the prcomp function in R.

Differential gene expression was determined using edgeR (Robinson and Oshlack, 2010). For heatmap visualization (Figure 2A), 7'626 genes (Table S1) were considered that were significantly regulated during control organoid formation (absolute Log2 fold gene expression change at d5, d7, d9, d11, d12 or d21 relative to iPSCs greater than Log2(3) with a false discovery rate (FDR) smaller than 0.001) or upon *WT1* KO (absolute Log2 fold expression changes in KO^{iPSC} or $KO^{d4\text{-}7}$ organoids relative to control organoids at any time point greater than Log2(3) with a FDR smaller than 0.001).

For comparison with published kidney organoid gene expression (Wu et al., 2018) (GSE118184) (Figure S1C), scRNAseq reads of 218 iPSCs and of 25120 (Morizane protocol) and 82024 (Takasato protocol) cells from d26 organoids were summed and normalized, and Log2 fold expression changes relative to iPSCs were calculated using a pseudocount of 1. Correlation coefficients are based on 12817 genes detected in (Wu et al., 2018) and the RNA-seq dataset reported in this work. Pearson correlation coefficients were calculated using R's *cor* function.

For generation of gene-set overlap scores (Figure 2C), we first calculated the odds-ratio for each pairwise comparison between embryonic kidney gene sets (Lindström et al., 2018) and gene clusters 1-17, using the *fisher.test* function in R. To correct for biases introduced by different gene-set sizes, each observed odd-ratio was then normalized by calculating a Z-score: $z\_score = \frac{obs - mean\_rand}{sd\_rand}$, where obs is the observed odds-ratio for a given pairwise comparison, and mean_rand and sd_rand are the mean and standard-deviation of 100 randomized odd-ratios, obtained from equal-sized sets of randomly selected genes.

Analyses of enriched gene sets (Figure S3F,H and Table S1,S2) was performed using DAVID (Huang et al., 2008) and selecting GOTERM_BP_ALL.

Single-cell RNAseq (scRNAseq) datasets of week 16 fetal kidney scRNAseq (Hochane et al., 2019) (GSE114530) were integrated with and contrasted to the results of this study. For the analysis and visualization of the scRNAseq data (Figures 2D) we filtered out genes detected in < 1% of the cells as well as the abundantly expressed and noisy ribosomal protein genes. From the remaining fraction, only the top 5% overdispersed genes were selected as input for the downstream dimensionality reduction and dataset integration methods according to a mean-variance trend fit using a semi-parametric approach (Zheng et al., 2017).The coordinates of the first 32-principal components were used to obtain the 2D tSNE representation of the data. For visualization purposes per-cell gene expression values were subjected to k-nearest neighbor smoothing (k=64) and normalized against a random set of 2000 detected genes in order to control for artefactual expression gradients.

For transcriptional changes in kidney cancer patients (Figure 3, S3G-I), Wilms tumor (WT; Gadd et al., 2017), Kidney Chromophobe Carcinoma (KIRC; TGCA; Davis et al., 2014), Kidney Papillary Cell Carcinoma (KIRP; The Cancer Genome Atlas Research Network, 2016), and Kidney Clear Cell Carcinoma (KIRC; TCGA; Creighton et al., 2013) datasets (TARGET-WT, TCGA-KICH, TCGA-KIRP, and TCGA-KIRC) were downloaded from GDC (https://portal.gdc.cancer.gov) using the TCGAbiolinks package available from Bioconductor. Data sets were normalized, and Log2 fold expression changes for each sample calculated over the mean of the respective control samples using a pseudocount of 1. Wilms tumor expression affymetrix data (Gadd et al., 2012) (GSE31403) were downloaded using *getGEO* from the Bioconductor package GEOquery, Log2 transformed, in case of multiple probe sets per gene the probe set with the highest average value across samples selected, and normalized to the mean expression in all patients (mean-centered). Only patients assigned to subsets S1 – S4 (Gadd et al., 2012) in this dataset were considered.

Wherever indicated, Log2 fold gene expression changes were scaled using the *scale* function with the parameters *center = FALSE* and *scale = TRUE* (scaled Log2 fold expression changes) to allow comparison between datasets from different studies.

Pairwise Pearson correlation coefficients in Figure 3B were calculated using R's *cor* function, and are of 24920 genes and between scaled mean Log2 fold expression changes in d21 KO^{iPSC} and $KO^{d4\text{-}7}$ organoids and scaled mean Log2 fold expression changes in TARGET-WT, TCGA-KICH, TCGA-KIRP and TCGA-KIRC patients.

For heatmap visualization in Figure S3G, 2100 genes with a scaled Log2 fold expression change of greater than 3 in at least one of the patients were considered (Table S2).

Cell type markers (Figure S3B) were selected from the literature, while EMT signature genes (Figure S3D) are the 38 genes in the EMTome database (Vasaikar et al., 2021) that have literature support (Vasaikar et al., 2021) and showed an absolute Log2 fold expression change between not-edited d21 and d9 organoids of greater than 2.

Unsupervised clusterings in Figures S1E (Log2 normalized counts), 3A (Log2 fold expression changes), and 3B,C,D (scaled Log2 fold expression changes) were performed using the *aheatmap* function from the Bioconductor package NMF, and in Figures 3D, S3G (scaled Log2 fold expression changes) and 3E (Log2 fold expression changes) using the Heatmap function from the Bioconductor package ComplexHeatmap. We named the patient cluster identified by unsupervised clustering in Figure S3G "myo_subset" as it correlated with strong expression of WTPGC 3 genes that are enriched for muscle genes (Figure 3D) and muscle terms (Figure S3H).

SUPPLEMENTAL REFERENCES

Choi, J., Lee, S., Mallard, W., Clement, K., Tagliazucchi, G.M., Lim, H., Choi, I.Y., Ferrari, F., Tsankov, A.M., Pop, R., et al. (2015). A comparison of genetically matched cell lines reveals the equivalence of human iPSCs and ESCs. Nat Biotechnol *33*, 1173–1181.

Gadd, S., Huff, V., Huang, C.-C., Ruteshouser, E.C., Dome, J.S., Grundy, P.E., Breslow, N., Jennings, L., Green, D.M., Beckwith, J.B., et al. (2012). Clinically Relevant Subsets Identified by Gene Expression Patterns Support a Revised Ontogenic Model of Wilms Tumor: A Children's Oncology Group Study. Neoplasia *14*, 742-756.

Gaidatzis, D., Lerch, A., Hahne, F., and Stadler, M.B. (2015). QuasR: quantification and annotation of short reads in R. Bioinformatics *31*, 1130–1132.

Hochane, M., Berg, P.R. van den, Fan, X., Bérenger-Currias, N., Adegeest, E., Bialecka, M., Nieveen, M., Menschaart, M., Lopes, S.M.C. de S., and Semrau, S. (2019). Single-cell transcriptomics reveals gene expression dynamics of human fetal kidney development. Plos Biol *17*, e3000152.

Huang, D.W., Sherman, B.T., and Lempicki, R.A. (2008). Bioinformatics enrichment tools: paths toward the comprehensive functional analysis of large gene lists. Nucleic Acids Res *37*, 1–13.

Kogut, I., McCarthy, S.M., Pavlova, M., Astling, D.P., Chen, X., Jakimenko, A., Jones, K.L., Getahun, A., Cambier, J.C., Pasmooij, A.M.G., et al. (2018). High-efficiency RNA-based reprogramming of human primary fibroblasts. Nat Commun *9*, 745.

Lindström, N.O., Brandine, G.D.S., Tran, T., Ransick, A., Suh, G., Guo, J., Kim, A.D., Parvez, R.K., Ruffins, S.W., Rutledge, E.A., et al. (2018). Progressive Recruitment of Mesenchymal Progenitors Reveals a Time-Dependent Process of Cell Fate Acquisition in Mouse and Human Nephrogenesis. Dev Cell *45*, 651-660.e4.

Liu, Z., Lou, H., Xie, K., Wang, H., Chen, N., Aparicio, O.M., Zhang, M.Q., Jiang, R., and Chen, T. (2017). Reconstructing cell cycle pseudo time-series via single-cell transcriptome data. Nat Commun *8*, 22.

Morizane, R., Lam, A.Q., Freedman, B.S., Kishi, S., Valerius, M.T., and Bonventre, J.V. (2015). Nephron organoids derived from human pluripotent stem cells model kidney development and injury. Nat Biotechnol *33*, 1193–1200.

Robinson, M.D., and Oshlack, A. (2010). A scaling normalization method for differential expression analysis of RNA-seq data. Genome Biol *11*, R25.

Theunissen, T.W., Friedli, M., He, Y., Planet, E., O'Neil, R.C., Markoulaki, S., Pontis, J., Wang, H., Iouranova, A., Imbeault, M., et al. (2016). Molecular Criteria for Defining the Naive Human Pluripotent State. Cell Stem Cell *19*, 502–515.

Ungricht, R., Guibbal, L., Lasbennes, M.-C., Orsini, V., Beibel, M., Waldt, A., Cuttat, R., Carbone, W., Basler, A., Roma, G., et al. (2021). Genome-wide screening in human kidney

organoids identifies novel aspects of nephrogenesis. bioRxiv, doi: 10.1101/2021.05.26.445745

Vasaikar, S.V., Deshmukh, A.P., Hollander, P. den, Addanki, S., Kuburich, N.A., Kudaravalli, S., Joseph, R., Chang, J.T., Soundararajan, R., and Mani, S.A. (2021). EMTome: a resource for pan-cancer analysis of epithelial-mesenchymal transition genes and signatures. Brit J Cancer *124*, 259–269.

Villegas, F., Lehalle, D., Mayer, D., Rittirsch, M., Stadler, M.B., Zinner, M., Olivieri, D., Vabres, P., Duplomb-Jego, L., Bont, E.S.J.M.D., et al. (2019). Lysosomal Signaling Licenses Embryonic Stem Cell Differentiation via Inactivation of Tfe3. Cell Stem Cell *24*, 257-270.e8.

Wu, H., Uchimura, K., Donnelly, E.L., Kirita, Y., Morris, S.A., and Humphreys, B.D. (2018). Comparative Analysis and Refinement of Human PSC-Derived Kidney Organoid Differentiation with Single-Cell Transcriptomics. Cell Stem Cell *23*, 869-881.e8.

Zheng, G.X.Y., Terry, J.M., Belgrader, P., Ryvkin, P., Bent, Z.W., Wilson, R., Ziraldo, S.B., Wheeler, T.D., McDermott, G.P., Zhu, J., et al. (2017). Massively parallel digital transcriptional profiling of single cells. Nat Commun *8*, 14049.